Fault migration and basin evolution during complex rifting: examples from the western North Gulf of Evia, Greece

James Wood[1], Rebecca E. Bell[1], Alexander C. Whittaker[1], Saoirse M. Coveney[1], Frank Chanier[2], Fabien Caroir[3], Haralambos D. Kranis[4], Athanassios Ganas[5]

[1] Department of Earth Science & Engineering, Imperial College London, London, UK

[2] Laboratoire d'Océanologie et de Géosciences, Univ. Lille, CNRS, Univ. Littoral Côte d'Opale, Lille, France

[3] Institut des Sciences de la Terre de Paris, Sorbonne Université, CNRS-INSU, Paris, France

[4] Department of Geology and Geoenvironment, National and Kapodistrian University of Athens, Athens, Greece

[5] Institute of Geodynamics, National Observatory of Athens, Athens, Greece

Corresponding author: James Wood (james.wood18@imperial.ac.uk)

Acknowledgements

This work received funding as part of the TALENTS doctoral network through the European Union's HORIZON-MSCA-2022-DN-01 research and innovation program under grant agreement No. 101119486 (https://www.talents-dn.eu). JW, AW, RB, HK, and AG are beneficiaries of this grant. SC is funded by NERC grant NE/S007415/1 (Science and Solutions for a Changing Planet DTN). We are grateful to SLB for the provision of Petrel (Version 2024.4.0) for use in this project. We are also grateful to the crews and scientific teams associated with the collection of the WATER seismic reflection data used in this study.

Abstract

Understanding dynamic processes of faulting and basin evolution across timescales in complex rift settings remains a key challenge in active continental tectonics. This is in part due to a limited number of young rift systems with well constrained, high-resolution age models derived from subsurface datasets. We aim to address this challenge and advance our understanding of time-dependent geodynamic rift processes by developing a late-Quaternary, syn-kinematic age model for the Western Basin of the North Gulf of Evia, Central Greece. In contrast to the nearby Gulf of Corinth, extension here is coupled with rotational and strike-slip deformation from the westward-propagating North Anatolian Fault. Seismic stratigraphic principles are used to identify three key horizons based on reflection termination relationships with ages of ~12 ka, ~130 ka and ~325 ka assigned through a sequence stratigraphic model on deltaic clinoform packages. The age model is applied alongside a network of offshore faults to determine the major structures, depocenters and evolutionary history of the rift. We resolve the major controlling faults to be the north-dipping Kalypso Fault (~4 mm/yr slip rate) at the southern margin of the basin and the Central Graben (~1-2 mm/yr slip rate) along the axis of the gulf. We show that the Kalypso Fault is linked to the onshore Coastal Fault System following a migration event with evolving strike from the onshore Arkitsa Fault. The timing of this event is constrained to ~325 ka based on hanging wall sediment thickening relationships and the Kalypso Fault displays immediate, rapid throw accumulation after initiation. Improved constraints on the timing and evolutionary behaviour of young normal fault systems such as this show that fault migration and activation in complex rift settings can occur over timescales less than 10^5 years.

Graphical Abstract

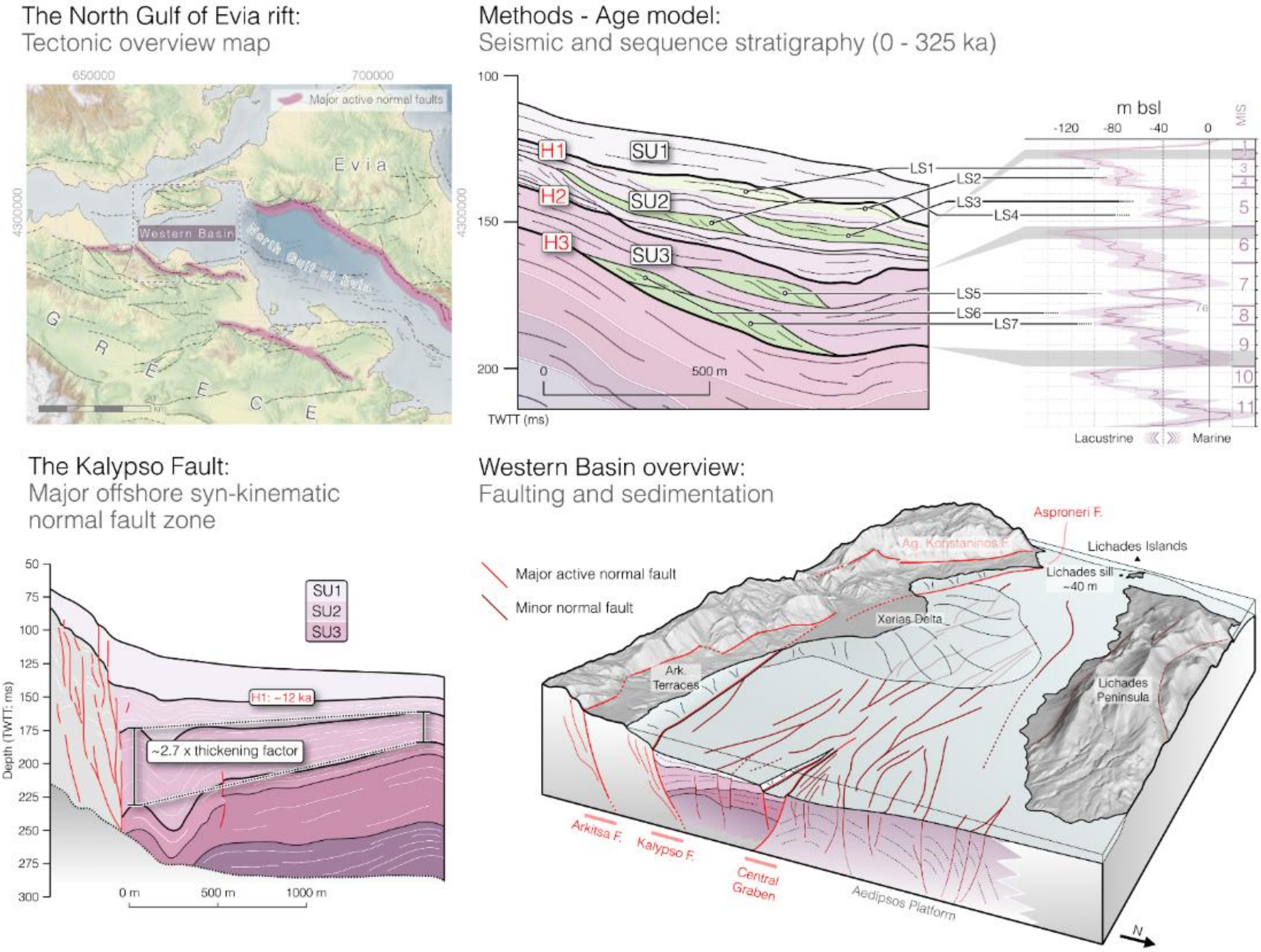

1. Introduction

Understanding the timing of fault initiation and strain localisation in rifts is of key importance for constraining models of continental extension, syn-tectonic basin evolution, and seismic hazard. However, as young continental rifts are some of the most dynamic tectonic systems on Earth (Brune et al., 2023), any detailed reconstruction of the timing of fault initiation, linkage and migration typically demands a high-resolution age model of syn-kinematic stratigraphy (Gawthorpe and Leeder, 2000). However, available age models in active rifts at sufficient detail to allow fault slip rates and timings of initiation, linkage and migration to be resolved over high-resolution timescales (10^3-10^4 years) are sparse.

Rifting is rarely a simple process as fault systems may develop oblique to extensional strain (e.g., Agostini et al., 2009; Brune, 2014; Jourdon et al., 2020), basement inheritance can influence fault growth and migration (e.g., Brune et al., 2017; Molnar et al., 2017; Phillips et al., 2019), and crustal block rotation can introduce evolving principal stress orientations in the rift (e.g., Bradley et al., 2013; Zwaan et al., 2020; Zwaan and Schreurs, 2020). Temporal and spatial reconstructions of normal fault dynamics from natural examples in active complex and rotational rift settings are limited at present. For example, vertical-axis block rotation in New Zealand has controlled the V-shaped normal fault propagation observed in the Taupo Rift (Schmid et al., 2022; Villamor et al., 2017; Wallace et al., 2004), and anticlockwise rotation of the Arabian Plate away from the Afar Rift, Ethiopia has generated a sequence of obliquely migrating normal fault zones (Zwaan et al., 2020a). While rift-scale geodynamic processes are resolved on timescales of 10^5-10^6 years in these settings (e.g., Chandresh et al., 2026; Villamor et al., 2017; Zwaan et al., 2020b), these complex rifts lack the density and resolution of subsurface datasets currently found in orthogonal settings, such as the Gulf of Corinth (e.g., McNeill et al., 2019; Nixon et al., 2016), or moderately oblique systems, such as Lake Malawi (e.g., Lyons et al., 2011), where seismic reflection data and drilling have allowed analyses of deformation and sedimentation at 10^4-10^5 year timescales (e.g., McNeill et al., 2026).

Syn-rift sedimentation in evolving basins, typically imaged at depth with seismic reflection data, provides an integrated, but often complex, record of both tectonic and environmental forcing (Gawthorpe and Leeder, 2000). However, where tectonic signals can be isolated effectively, for instance through the reconstruction of prevailing environmental conditions (e.g., base level), analysis of syn-rift stratigraphy can provide powerful, quantitative insights into slip rates and evolution of normal fault systems (e.g., Bell et al., 2009, 2008; Feng et al., 2016; Gawthorpe et al., 2018; Nixon et al., 2024, 2016).

Resolving the interplay between tectonic structure and sedimentation can also provide important insight into the prevailing geodynamics of active rifts (Gawthorpe and Leeder, 2000). For example, a localised (i.e. linked) border fault in an orthogonal rift is typically expected to host a major depocenter at the centre of the linked array (e.g., Cowie et al., 2006; Nixon et al., 2016). Where transverse strike- and oblique-slip fault belts intersect active rifts, sedimentary depocenters may be asymmetrically distributed or segmented along the rift axis (e.g., Laó-Dávila et al., 2015; Scholz et al., 2020). Equally, strike-slip structures in composite extensional and strike-slip arrays can host ancillary sedimentary basins in negative flower structures and transtensional basins (e.g., Huang and Liu, 2017; Yilmaz et al., 2025). In contrast, if rifting is coupled with vertical-axis block rotation, major syn-sedimentary normal fault zones propagate radially about a rotational axis in a characteristic V-shaped geometry (e.g., Schmid et al., 2022; Zwaan et al., 2020b). Detailed integrated analysis of both the structural fabric and sediment distribution of active rift systems can therefore provide key constraints on the evolution of complex and composite deformation regimes over time.

The North Gulf of Evia, located in Central Greece, provides an ideal natural laboratory for the study of active rift processes at the interface of extension and propagating shear deformation (Figures 1a and 1b; Caroir et al., 2024; Chousianitis et al., 2024; Sboras et al., 2025). Although the rift system is dominantly characterised by major normal fault zones bounding the margin of the gulf (Figure 1b; Goldsworthy et al., 2002; Roberts and Ganas, 2000; Whittaker and Walker, 2015), extension is coupled with marked vertical-axis rotation (Bradley et al., 2013; Chousianitis et al., 2024) and active right- and left-lateral strike-slip deformation (Figure 1b; Ganas et al., 2016; Kranis et al., 2001; Palyvos et al., 2006; Sboras et al., 2025). The North Gulf of Evia therefore provides an excellent opportunity to advance our understanding of rifting and time-dependent normal fault processes when influenced by geodynamic complexity. However, no pre-Holocene seismic stratigraphic age model has been proposed for the syn-rift basin fill of the gulf to date, and borehole records are absent. Timing, slip rates, and the evolutionary history of important structures of this active rift system remain key unknowns.

It is also important to contextualise the North Gulf of Evia rift in comparison to the well-studied Gulf of Corinth Rift, located ~50 km south (Figure 1c). Although these systems share some key characteristics (e.g., regional geodynamic and climatic histories) and are located in the same principal extensional regime (e.g., Chousianitis et al., 2024, Figure 1b-c), the Gulf of Corinth is considered a broadly orthogonal rift system with limited influence from strike-slip deformation (Bell et al., 2009; Gawthorpe et al., 2018; Roberts and Koukouvelas, 1996). Moreover, the geometry of major normal fault zones can be seen to vary markedly between the Gulf of Corinth and the North Gulf of Evia, as illustrated in the simplified structural maps of Figure 1b-c.

The Gulf of Corinth benefits from being one of the only continental rift systems with a high-resolution, validated age model owing to extensive seismic reflection datasets (see Nixon et al., 2016) and offshore drilling (McNeill et al., 2019; Nixon et al., 2024). The age models developed in the Gulf of Corinth generated a framework for the rift to become one of the foremost natural laboratories for the detailed study of normal faulting processes (e.g., Bell et al., 2017; de Gelder et al., 2019; Fernández-Blanco et al., 2019; Mildon et al., 2024) and basin sedimentation (e.g., Gawthorpe et al., 2017; McNeill et al., 2019; Watkins et al., 2018). Developing a comparable high-resolution correlated offshore age model for the North Gulf of Evia will allow dynamic rift processes to be studied in detail in a region of complex stress interactions and composite active deformation.

In this study we utilise a high-density, high-resolution 2D seismic reflection dataset to develop a consistent seismic and sequence stratigraphic age model for late-Quaternary syn-tectonic sedimentation (0 – ~325 ka) of the western North Gulf of Evia (Figure 2). We map a new offshore network of normal faults and apply the age model to reconstruct a detailed, late-Quaternary history of fault slip and basin development. Normal fault migration processes are examined in the context of vertical-axis rotation and strike-slip deformation in the region and in doing so, our work sheds new insight into the temporal evolution of complex rift systems over timescales of 10^4-10^5 years.

2. Geological Background

2.1 Tectonic setting

The North Gulf of Evia is one of a series of young, ~E-W striking rift systems spanning the continental block of mainland Greece (Figure 1a-c; Goldsworthy et al., 2002; Papanikolaou, 2021; Roberts and Ganas, 2000; Roberts and Jackson, 1991). Extension is thought to be controlled by the rollback of a shallowly subducting African Plate (Jolivet et al., 2013) with regional influence from the westward-propagation of the North Anatolian Fault and westward extrusion of the Anatolian Plate (Figure 1a; Caroir et al., 2024; Goldsworthy et al., 2002; Hatzfeld et al., 1999; Sboras et al., 2025). This influence is responsible for 5-8°/Myr clockwise rotation of the continental block between the gulfs of Evia and Corinth (Bradley et al., 2013; Briole et al., 2021; Chousianitis et al., 2024) and the strike- and oblique-slip deformation resolved in the North Gulf of Evia rift system inferred from earthquake focal mechanisms and geomorphic indicators (Figure 2a; Caroir et al., 2024; Ganas et al., 2016; Kranis et al., 2001; Palyvos et al., 2006).

Although modern geodetic opening rates of 2.9-3.7 mm/yr (Sboras et al., 2025) are ~4 times slower than in the neighbouring Corinth Rift (Figure 1b-c; Briole et al., 2021; Chousianitis et al., 2024), large, damaging earthquakes are known to have occurred around the North Gulf of Evia including the 1894 Atalanti events (Mw 6.4-6.9; Ganas et al., 1998; Pantosti et al., 2004) and the unattributed tsunami-generating earthquake of 426 BCE (Freitag and Reicherter, 2019).

The modern tectonic configuration of the North Gulf of Evia is divided into the Western, Central and Eastern Basins based on bathymetric and subsurface character (Sakellariou et al., 2007; Fig. 2a). Here we consider the Western Basin, a sub-basin at the margin of the gulf between the Coastal Fault System and the Lichades Peninsula (Figure 2b) with the highest extensional strain accommodation in the gulf (~3.7 mm/yr; Sboras et al., 2025). The Coastal Faults span from Arkitsa to beyond Kammena (*or Kamena*) Vourla (~30 km) as a segmented but linked onshore active normal fault array with a late-Quaternary footwall-component uplift rate of 0.2-0.6 mm/yr (Whittaker and Walker, 2015). The fault system is typically considered the most active structure of the modern rift (Goldsworthy et al., 2002; Roberts and Jackson, 1991). The segments of the Coastal Faults vary in orientation and dip but ubiquitously display north-oriented slip vectors (Figure 2b; Kranis 2007).

Despite evidence for Holocene slip on the Coastal Faults (Kranis, 2007), the geomorphology of the ~2 km wide strip of land between the main fault zone and coastline provides evidence for ongoing uplift in the hanging wall of the structure (c.f. Wood et al., 2025). This includes the uplifted marine terraces at Arkitsa (Figure 2b) and Holocene coastal notches at Kynos (Supplementary Figure S1), which may indicate the dominant normal faults have migrated offshore (Papanastassiou et al., 2014; Pirazzoli et al., 1999).

2.2 Pleistocene palaeoenvironment

Sedimentation in basins provides a record of prevailing relative sea, lake or river level (Vail et al., 1977). Isolating tectonic signals from the sedimentary packages imaged in seismic reflection data demands a comprehensive reconstruction of environmental conditions (e.g., base level, sill level and sedimentary environment).

The North Gulf of Evia is a semi-enclosed basin with distinct marine, lacustrine and brackish intervals over the late-Quaternary controlled by sills in the Oreoi and Lichades Straits at 40-45 m bsl (below mean sea level; Figure 2b). Intervals where eustatic sea level is below sill level are interpreted as lacustrine or brackish in the Gulf and eustatic highstands above ~40 m bsl are considered marine. It is probable that most of the Pleistocene lakes of the North Gulf of Evia were restricted to the deepest part of the basin where many submerged terraces have been mapped in vintage seismic datasets (Van Andel and Perissoratis, 2006).

The sill level at Lichades (Figure 2b) has likely varied over time. InSAR-derived ground motion data indicates ~1 mm/yr of uplift over 2019-2023 on the island of Lichades and the coastal land strip at Kammena Vourla (Wood et al., 2025). The shallowing of the sill has been independently inferred through analysis of Pleistocene microfossil assemblages (Drinia et al., 2014).

The main fluvial drainage of the rift system, the Sperchios River (Figure 2a) reflects a closed sedimentary system throughout the Holocene with all transported sediment deposited in its delta at the Maliakos Gulf (Pechlivanidou et al., 2018). During lowstand conditions, the river likely drained to the Aegean through the Oreoi Channel (Figure 2a), although it is possible that drainage fluctuated to the endorheic basin that hosted the North Gulf of Evia Pleistocene lakes where deltaic packages are resolved in seismic reflection data (Caroir et al., 2024; Van Andel and Perissoratis, 2006). The Western Basin therefore likely alternated between a sedimentary sink and fluvial transfer zone depending on prevailing base level and rate of accommodation generation.

3. Data and Methods

3.1 Seismic data and stratigraphic age model

A high density, high resolution seismic reflection dataset across the Western Basin is used to explore the sedimentary and tectonic development of the sub-basin in detail (WATER I and II; Chanier and Gaullier, 2017; Chanier and Watremez, 2021; Figure 2b, Supplementary Figure S5). The WATER surveys acquired ~1800 km of single channel sparker (50-300 J) seismic profiles across the North Gulf of Evia, Oreoi Channel and Skopelos Basin. The subset of 41 profiles used in this study are ca. 350 ms at maximum interpretable depth (~260 – 320 m) and data is typically interpreted to the first seabed multiple which obscures the signal below. Seismic velocities are modelled as 1500 m/s for seawater and 1800 m/s for depth conversions consistent with Caroir et al. (2024).

The WATER dataset has been studied previously to determine the regional structural anatomy of the North Gulf of Evia and show the influence of strike-slip deformation at the western termination of the North Anatolian Fault (Caroir et al., 2024). However, no pre-Holocene age correlations have been made for the sedimentary stratigraphy in the offshore North Gulf of Evia to date.

In this study, key seismic horizons (H1-H3) are identified in the dataset based on seismic terminations including onlap relationships and erosive truncation (Figure 3; Catuneanu, 2002; Vail et al., 1977). Between these horizons, seismic units (SU1-3) are defined and each unit is characterised based on seismic attributes and geological significance, consistent with seismic facies principles (Vail et al., 1977; Xu and Haq, 2022). Three-dimensional surfaces are produced from the key seismic horizons to analyse spatial variability of sediment package thickness across the gulf (Supplementary Figure S3) with isopachs for each SU calculated as the difference between two surfaces.

Age estimates for the seismic horizons and units are derived from sequence stratigraphic principles as unconformity-bounded sediment sequences at the margins of marine and lacustrine systems preserve a record of relative base level change (Catuneanu, 2002; Vail et al., 1977). In clastic systems at basin margins, deltas build up (i.e., aggrade) to prevailing base level before growing outwards (i.e. prograde). When preserved in the geologic record, these packages can be used to infer the sequential timing of local highstand and lowstand periods (Catuneanu, 2002). For late-Quaternary sedimentation, well constrained eustatic sea level curves (e.g., Spratt and Lisiecki, 2016) can be correlated to sequences of clinoforms to generate age models for basin sedimentation (e.g., Bell et al., 2008; Lykousis et al., 2007a).

In the south of the Western Basin, a well-developed sequence of submerged clinoform packages is found on seismic lines 107 and 049. We use these packages to establish age estimates for seismic horizons through correlation to the sea level curve of Spratt and Lisiecki (2016; Figure 3 and 4). We identify distinct clinoform package rollover points (i.e. topset to foreset transition) in seismic profiles which act as markers of past marine or lacustrine relative base level in the gulf (Catuneanu, 2002). To establish if a clinoform package best correlates to a highstand or lowstand interval, we consider package geometry, apparent base level and stratigraphic sequencing (Catuneanu, 2002; Figure 3a and 3b). We define packages as lowstands if they sit stratigraphically above a package with a higher indicated base level or show an exaggerated sigmoidal geometry consistent with decreasing/low accommodation (Figure 3a). We define sequences as highstands if they build up to higher base level than the underlying stratigraphic package (Figure 3b). Ages are provided with reference to Marine

Isotope Stages (MIS) and numeric values are assigned based on correlation to the sea level stack of Spratt and Lisiecki (2016).

Sill level is marked on base level diagrams at 40 m bsl and at a level consistent with an uplifting sill at 0.1 mm/yr (i.e. 10 year period of 1 mm/yr uplift every 100 years; Wood et al., 2025). We assume that base levels below sill height represent lacustrine intervals and above are considered marine. To generate the age correlation, we make the simplifying assumption that relative base level change between subsequent MIS substages is consistent across both lacustrine and marine periods according to the eustatic curve (Spratt and Lisiecki, 2016). This is in line with methods used to propose pre-drilling correlations in the Gulf of Corinth (e.g., Bell et al., 2008; Lykousis et al., 2007b), however some uncertainty is introduced by this assumption (see section 5.2 for further discussion).

3.2 Identification and classification of normal faults

We identify offshore faults in seismic reflection profiles and map these structures across lines to generate three-dimensional geometries. Structures are then classified on the most recent key seismic horizon (H1-H3) they offset, providing an estimate for most recent activity. We measure fault throw as the vertical offset of the key correlated seismic horizons defined in the age model across each structure which represents the maximum observable throw on each fault over the given time interval. Throw rates are converted to slip rates with an assumed fault dip of 60-70°, consistent with measured fault planes on the Arkitsa Fault (Kokkalas et al., 2007; Kranis, 2007). The full fault database is summarised in more detail in the supplementary material (Figure S4; Table S1 and S2).

Geological field work was conducted in April and October 2025 and included corroborating previous works, refining onshore fault maps (Figure 2) and documenting evidence for onshore uplift and young normal faulting within syn-rift stratigraphy (Supplementary Figure S1).

4. Results

4.1 Seismic stratigraphy

Three major stratigraphic horizons are identified based on the observation of erosional truncation, onlap terminations and significant changes in seismic character (H1, H2 and H3). These surfaces can be seen on the seismic profiles of Figure 3c and 4 and their character is summarised in Figure 5.

Both H1 and H2 are highly erosive with overlying sediments commonly onlapping these surfaces (Figures 3 and 4). These horizons each represent a depositional hiatus in the gulf, representing extended periods of subaerial erosion when the North Gulf of Evia lake was restricted to the deep Central Basin (Van Andel and Perissoratis, 2006).

A significant change in seismic facies occurs across surface H3 (Figure 5). Younger, overlying sediments are dominated by high amplitude reflectors and abundant clinoforms while below H3, reflections are dominantly low amplitude punctuated by thin, high amplitude packages (Figures 5 and 6). In places, overlying reflections onlap H3 (Figure 6b).

H1 to H3 bound three seismic units defined in Figure 4 (SU1-3). SU1 is found between the seabed and H1. It is dominated by acoustically transparent fan deposits with a thin, high amplitude drape elsewhere. SU1 is equivalent to the Upper Sequence of Caroir et al. (2024) which is considered to represent Holocene sedimentation in that study. Shallow coring of this seismic unit in the Central Basin has confirmed the Holocene age of these sediments (Drinia et al., 2014; Sakellariou et al., 2007). The fan deposits that dominate the Western Basin are derived from the Xerias River (Figure 2b; Van Andel and Perissoratis, 2006). The erosive surface H1 therefore formed during the Last Glacial Maximum (MIS 2, before 12 ka) and represents the base of Holocene deposition.

SU2 is found between H1 and H2. It is highly variable in thickness, owing to erosive surfaces at both the base (H2) and top (H1) of the unit and is characterised by abundant clinoforms and onlapping reflectors (Figure 5 and 6). The reflections in the unit are typically high amplitude which, based on seismic reflections and age correlations in the Gulf of Corinth (e.g., Bell et al., 2008; Nixon et al., 2016), implies highstand conditions dominate sedimentation during this time.

SU3, between H2 and H3, is similarly characterised by high amplitude reflections but tends to be more laterally continuous and lower frequency than SU2 with fewer clinoforms (Figure 4). The unit, in deeper basin settings transitions from high amplitude to low amplitude while in marginal depositional settings is nearly exclusively high amplitude with abundant internal and external onlap relationships (Figure 6). SU3 unit is interpreted to represent highstand sedimentation in a marginal sub-basin prior to subaerial exposure and the formation of H2.

4.2 Sequence stratigraphy

Sequence stratigraphy of deltaic clinoform packages in Figure 2 and 3 is used to attribute ages to the seismic stratigraphy outlined above through correlation to expected base level in the gulf. Within the sedimentary succession spanning H1 to H3 shown in Figure 3c and 3d, nine distinct packages are identified. Based on the ordering of apparent relative base levels and sequence geometries outlined in the schematic diagrams of Figure 2a and 2b, each package is classified as a relative lowstand or highstand.

Seven lowstand indicators are interpreted between 98 and 135 m bsl (LS1-LS7). These packages have cross-sectional widths of 200-600 m with heights of ~10-20 ms (~9-18 m).

LS1 and LS2 sit directly below H1 and indicate similar relative base levels of 98 and 109 m respectively. As H1 very likely represents the base-Holocene surface (see section 4.1), these clinoforms must have developed during moderately high lake level or brackish deposition in MIS 3 at a base level between sill level and ~-80 m bsl (Figure 3d). Lake levels in both MIS 2 and MIS 4 were restricted to the Central Basin (Figure 2b; Van Andel and Perissoratis, 2006) so deltaic clinoforms are unlikely to have developed in this part of the Western Basin during those intervals.

HS1, LS3, HS2 and LS4 follow in the stratigraphic sequence and compose the remaining strata of SU2. HS1 and HS2 are interpreted as highstands as both aggradation of >40 m and retreat towards the basin margin of ~1.2 km are resolved for these packages (see comparison to Figure 3b). The rollover of HS1 is not imaged here so the apparent relative base level of ~70 m bsl is considered a minimum possible value. LS3 (~118 m bsl) sits stratigraphically above HS1 while LS4 (~114 m bsl) sits between HS1 and HS2 with the morphologies and stratigraphic relationships of the two lowstand patterns indicative of a forced regression (see comparison to Figure 2a). The downdip extension of the HS1 package bifurcates above and below LS3 while the up-dip extent of this unit drapes HS2. Based on this sequencing, these four packages are attributed to MIS 5 with HS2 being MIS 5e and the thin sediment drape above this of HS1 likely being an amalgamation of MIS 5c and 5a. Significant local subsidence between MIS 5e and 5c is required to allow this drape at a sea level that is expected to be ~25 m lower than the extreme highstand of MIS 5e (Figure 3d). Based on sequencing relationships to these highstands, LS3 is attributed to MIS 5b and LS4 assigned to MIS 5d (Figure 3d).

Horizon H2 is located below this and, given its character as a strongly erosive surface, best represents late-MIS6 when the Western Basin likely saw an extended period of subaerial exposure following significant base level fall. Immediately below this surface is a package of consistent deposition without a preserved associated clinoform package (Figure 3c). LS5 (~126 m bsl) is a laterally restricted clinoform package with an indicated relative base level far below the underlying unit. It is therefore considered a lowstand interval (Figure 3a). LS6 (~125m bsl) is a narrow (~200m) clinoform set that builds up above the underlying package (LS7; ~135 m bsl). However, it does not build up above horizon H3 and, given aggradation from LS7 to LS6 is only ~10 m, both are considered lowstand packages. The stratigraphic positioning of LS5 best fits a moderate lowstand during MIS 7 (MIS 7d) with overlying sediment representing subsequent periods of higher sea level (i.e., MIS 7c-a). Finally, the two closely related packages of LS6 and LS7 sit below a further interval of highstand sedimentation (MIS 7e) and are best correlated to MIS 8.

Surface H3 marks the base of the interpreted clinoform packages in Figure 3c and 3d and, given its nature as a cap to a high amplitude package marking a significant change in basin sedimentation, is attributed to MIS 9e (Figure 3d). Correlation below H3 is uncertain due to poor imaging in the seismic reflection dataset across the basin.

Figure 4a shows a well-developed sequence of clinoforms on an intersecting seismic profile to Figure 3c (Figure 4b). All packages marked in Figure 4a are characterized as lowstand intervals based on comparison to expected geometries (Figure 3a) with two packages developed on the southeastern margin and four developed on the northwestern margin of a small paleo-bathymetric depression. Stratigraphic sequencing here is comparable to Figure 3c and all lowstand packages from Figure 3c are represented in this adjacent line, except LS2 which is not locally developed. Indicated base levels in Figure 3a are within 10% of counterparts in Figure 3c for each resolved lowstand package except LS1 which has an indicated depth of 17 m lower. This may imply heightened tectonic subsidence has occurred at the southeastern end of this profile.

Based on this sequence stratigraphic model across both Figure 3 and 4, age estimates of H1-3 and SU1-3 are derived and attributed to the seismic stratigraphic architecture of Figure 5. In short, H1 represents MIS 2 (~12 ka), H2 represents late-MIS 6 (~130 ka) and H3 represents MIS 9e (~325 ka).

Key to the utility of the age model is that it can be mapped consistently across the Western Basin and wider North Gulf of Evia. Figure 6 shows interpreted seismic profiles that span the axial length of the Western Basin (Figure 6a) and cross the width of the study area (Figure 6b) with the age model of Figure 5 applied. The erosive nature of H1 and H2 and the acoustic transparency of SU1 are well highlighted in Figure 5a and the onlapping relationships of H1-3 are highlighted in the south of Figure 6b. The marked change in seismic expression beneath horizon H3 is evident in across both profiles with a shift from high amplitude reflections dominating above to low amplitude reflections below. Where apparent in Figure 6a, clinoforms are restricted to SU2 and SU3 with indicated paleo-flow directions to the west. A substantial (~2 km wide) clinoform package attributed to MIS 5e on line 229 also indicates flow to the west. These flow directions are opposed to expected drainage to the southeast based on modern depocenters (Figure 2).

4.3 Normal fault network

Application of the age model to develop a full tectonic evolutionary history of the Western Basin demands a comprehensive map of offshore normal faults. Figure 7a and 7b show the mapped offshore fault network from this study. 47 offshore fault segments are mapped with lengths of 0.5 km to 12 km (see Supplementary Table S1 and S2). The structural fabric of the offshore rift is characterised by dominantly E-W striking normal faults, following the axis of the gulf (Figure 7). The density of sub-parallel normal faults across the width of the gulf increases from west to east as 3 to 4 structures span the basin near Neochori and 16 faults are mapped across the basin in the east (Figure 7a).

The base-Holocene surface (i.e. depth to H1 erosive surface) shown in Figure 7a and 7b provides a clearer indication of Pleistocene depocenters of the basin than modern bathymetry as the thick fan deposits from the Xerias River (Figure 2b) are stripped away. This surface allows primary depocenter-controlling structures to be identified.

The fault network in Figure 7a is classified on most recent evident fault slip derived from the youngest mapped horizon (H1-3) that they offset. Active faults (i.e. structures that offset H1 or the seabed) are depicted in red while faults that do not offset H1, H2 or H3 are considered least active (grey). Figure 7b classifies each structure on the maximum resolved throw rate in this study with separate rates calculated between each age-attributed horizon (Figure 5). Only three faults exhibit throw rates of >0.75 mm/yr (F01, F08 and F10) with the highest throw rate in the basin of ~3.75 mm/yr during the Holocene resolved for F01. Across all normal faults, a median throw rate of 0.2 mm/yr is resolved.

The southeast of the Western Basin appears to be controlled by a single, east-northeast striking (~260°) major normal fault zone (F01), here named the Kalypso Fault (from the homonymous settlement west of Arkitsa; Figure 7a). At the eastern tip of the fault, spacing to the onshore Arkitsa Fault segment is ~4 km with negligible spacing between the structures in the west, particularly when the onshore continuation of the fault is considered (Figure 7a). A potentially active normal fault had previously been inferred here based on the uplifted marine terraces between the Arkitsa Fault and the modern coastline (Cundy et al., 2010; Papanastassiou et al., 2014) and the fault is mapped as WB4 in the regional structural analysis of Caroir et al. (2024). We find the onshore continuation at the western extent of the

Kalypso Fault to follow a topographic escarpment (Figure 7) where fault breccia with syn-rift clasts and fault surfaces (79/025; dip/dip direction) are found (Supplementary Figure S1a).

The Central Graben, consisting of a major south dipping and north dipping normal fault (F10 and F08), is located along the axis of the gulf in the east of the study area (Figure 7). The graben opens significantly to the east with a fault spacing of 200 m at the western tip of the graben and > 2.5 km in the east (Figure 7a). The main faults of the graben appear to trend further to the east to bound the deep Central Basin, suggesting the faults are a significant modern bathymetric control in the gulf (c.f., Caroir et al., 2024). Slip is considerable on these structures with Holocene throw rates of 0.9 mm/yr on the south dipping fault and 1.7 mm/yr on the north dipping fault (Figure 7b).

The Asproneri Fault (F43) in the southwest generates a significant bathymetric escarpment and appears to be a major control on accommodation generation in this area (Figure 6b and 7a). This structure is likely responsible for uplifted terraces in the hanging wall of the onshore Agios Konstantinos Fault (Figure 2b; Supplementary Figure S1c). However, slip rates and along-strike variation for this structure are poorly resolved due to the low density of seismic profiles here (Figure 2b).

4.4 Syn-kinematic sedimentation

Integrating the sedimentary age model with the normal fault network in Figure 6 constructs a picture of how major depocenters in the Western Basin have changed over time in response to tectonic and environmental forcing. The syn-tectonic thickening of sediment packages into the hanging wall of normal faults also provides an indication of timing, and rates, of fault activity as hanging wall subsidence generates heightened accommodation space (e.g., Coveney et al., 2025; Gawthorpe and Leeder, 2000; Jackson et al., 2017). Figure 8 shows sediment isopachs of the three seismic units defined in Figure 5 (SU1-3) with the thickening direction of each unit SU1-3 indicating the major structural controls on syn-rift sedimentation at the time.

Figure 8a depicts a Holocene-only (SU1) isopach. In the west, sedimentation is dominated by the ~50 m thick deposits of the Xerias Fan, while in the east, Holocene sedimentation is thickest between the Kalypso Fault and a south-dipping series of faults ~3 km to the north (F02, F03, F46 – Figure 7). Elsewhere in the Western Basin, a thin drape of SU1 caps the underlying succession.

Figure 8b shows the thickness of SU2. This isopach also shows thickening towards the south and the Kalypso Fault to a maximum thickness of ~30 m. Yet, preserved sediment thickness of SU2 shows high variability due to an apparently wider spatial distribution of active faulting during this time and erosion from the overlying H1 unconformity.

Figure 8c also shows significant thickening of SU3 to the south across both the east, towards the Kalypso Fault, and west, towards the Asproneri Fault. Post-depositional faulting and subaerial erosion during MIS 6 (H2) and MIS2 (H1) results in similarly high variability in this isopach to Figure 8b. We hypothesise that the high variability in depocenter distribution towards the axis reflects some strike-slip offset, given the expected presence of oblique-slip in the rift system inferred from focal mechanisms (Caroir et al., 2024; Ganas et al., 2016; Sboras et al., 2025). However, the nature of 2D seismic reflection data does not permit detailed analysis of the oblique component of slip on these structures at this intra-basin scale.

Figure 8d shows a further isopach constructed from a pre-325 ka sediment package that is only correlated across the deeper southeast of the study area due to poor imaging elsewhere. In contrast to the overlying units, this package shows a thickening trend towards the north, showing an inverted polarity of thickening. This implies that the major control on accommodation generation in the depocenter during this interval was likely the south-dipping fault of the Central Graben (Figure 8d and 9).

These sediment thickening trends are also depicted in profile in Figure 9. Here, SU1-3 show significant syn-tectonic thickening into the immediate hanging wall of the Kalypso Fault. SU3, for example thickens from 20 m to 54 m over 1.5 km towards the fault zone (Figure 9b). Packages below SU3, such as the pre-325 ka package mapped in the isopach of Figure 8d, maintain constant thickness into the Kalypso fault plane and instead thicken significantly towards the Central Graben in the north (Figure 9a and 9b). This provides evidence that the Kalypso Fault likely initiated to become the dominant syn-sedimentary control on the Western Basin immediately prior to the deposition of SU3 (~325 ka).

Syn-kinematic thickening in Figure 9 appears to begin immediately above H3 with no marked change in sediment thickening rate between or within the units above and limited evidence of erosional truncation is observed in this part of the basin. This implies that the establishment of the Kalypso Fault as a high slip rate structure occurred rapidly over timescales of ~10^5 years with no gradual increase in slip rate observed in the syn-kinematic sedimentary record (Figure 9).

Figure 9a also directly images the fault zone of the Kalypso Fault. From the offset of the ~12 ka surface across the Kalypso Fault (~45 m) in this profile, a maximum Holocene throw rate of ~3.75 mm/yr is resolved (Figure 9b). Considering a long-term uplift to subsidence ratio of 1:2-3, consistent with normal faults in the Gulf of Corinth (e.g., Armijo et al., 1996; McNeill et al., 2005; Nixon et al., 2024), the Kalypso Fault is likely responsible for ~0.9-1.3 mm/yr footwall uplift. This is comparable to the estimated 1-1.5 mm/yr uplift rates derived for the Arkitsa marine terraces in the immediate footwall of the Kalypso Fault, based on ^{14}C dating of shelly fauna (Papanastassiou et al., 2014).

Other faults between the Kalypso Fault and Central Graben are resolved in the profile of Figure 9 but throw on these structures appears to be far less significant (<0.75 mm/yr; Figure 7b). However, the fault damage zone of F02 in Figure 9b has a geometry consistent with a negative flower structure, a structural style typical of oblique- or strike-slip deformation (Harding, 1985; Huang and Liu, 2017). Although resolving lateral displacement on this structure is restricted by the nature of the 2D seismic data used in this study, this fault zone provides some indication of rift-axial strike-slip developed in the Western Basin. However, the scale of the flower structure associated with F02 is small (~200 m across) and this fault does not appear to impact syn-kinematic depositional trends in this part of the gulf.

5. Discussion

5.1 Pleistocene evolution of the Western Basin

This study proposes the first late-Pleistocene age model for the North Gulf of Evia rift (Figure 5) and represents one of the first syn-kinematic subsurface age models in an active rift where extension is strongly coupled with strike-slip deformation. This age model provides high-resolution temporal constraints on syn-rift offshore deposition and, when combined with the new, detailed fault network of this study, offers the first estimates of Pleistocene slip rates on the offshore faults of the North Gulf of Evia (Figure 7). These new temporal and spatial constraints on the joint structural and paleoenvironmental evolution of the North Gulf of Evia have allowed several key events in the late-Pleistocene history of the offshore Western Basin to be resolved. These are presented in the schematic evolutionary block models of Figure 10a-c.

The initiation of the Kalypso Fault at ~325 ka, depicted in Figure 10a, represents a marked change in the major depocenter geometry and structural control in the gulf with older sedimentary units showing thickening towards the axial Central Graben (Figure 8d).

Following this, base level fall and subaerial exposure of the Western Basin resulted in significant erosion (H2) and drainage reorganisation during late-MIS 6 (~130 ka; Figure 10b). A similar significant regression occurred in the gulf during MIS 2, allowing the erosive H1 seismic surface to develop (Figure 5). During these extreme lowstand intervals, the studied area represents a fluvial transfer zone for drainage towards the main sedimentary sink of the rift system in the Central Basin (Figure 10b). This represents a key contrast to the Gulf of Corinth where basin geometry and depocenters are largely consistent across both lacustrine and marine intervals (Gawthorpe et al., 2018; Nixon et al., 2016). The dominant westward paleo-flow direction of clinoform packages in SU1 and SU2 of Figure 6a (opposite to modern drainage) suggests that drainage reorganisation has been a common occurrence in the Western Basin throughout the late-Pleistocene.

Subsequent flooding of the basin in the Holocene has promoted the rapid progradation of the Xerias Delta, which has dominated Western Basin deposition over the Holocene (Figure 8a, 10c and 10d).

5.2 Age model uncertainty and comparison to the Gulf of Corinth age model

Despite the broad applicability of the combined seismic and sequence stratigraphic age model developed here, the lack of available independent constraints on sediment age from offshore drilling in the North Gulf of Evia means several assumptions have been made to attribute the ages outlined in Figure 5.

The sill level linking the North Gulf of Evia to the Aegean Sea is an important source of uncertainty. While the modern Lichades Sill is found at a depth of ~40 m bsl (Caroir et al., 2024; Van Andel and Perissoratis, 2006), recent tectonic uplift suggests this level may be variable in the Quaternary (Wood et al., 2025) and the late-Pleistocene shallowing of the sill is independently inferred from analysis of microfossil assemblages in the Eastern Basin (Drinia et al., 2014). Where packages beneath the correlated age model are imaged (i.e., below H3), they typically do not show evidence of erosive truncation as seen across SU1-3 (e.g., Figure 6). This implies depositional sensitivity is reduced over this interval, most likely the result of a deeper sill prior to H3 (~325 ka). We depict a scenario with a consistent 0.1 mm/yr shallowing of the sill on the correlated sea level curves of Figures 3d, 5 and 6, however the precise timings of late-Pleistocene lacustrine isolation of the gulf remain poorly constrained.

A further assumption made is that relative lake level in the gulf between marine isotope substages is consistent with relative eustatic change between these same intervals. Highstand correlations (e.g., MIS 5, Figure 3c) carry the least uncertainty as it is expected the North Gulf of Evia is connected to the wider Mediterranean, and thus eustatic sea level, during these intervals while lowstand lacustrine deltas may form when lake level is decoupled from eustatic base level. Therefore, the substage correlations depicted in Figure 3c introduce a greater degree of uncertainty than the major correlated horizons that we map across the basin (Figure 5).

The base-Holocene horizon (H1) of our age model is consistent in character across a number of studies (Caroir et al., 2024; Sakellariou et al., 2007; Van Andel and Perissoratis, 2006) so the attribution of sediment directly overlying this unconformity to ~12 ka, when eustatic sea level last exceeded sill level (Spratt and Lisiecki, 2016), carries a relatively high degree of certainty. Shallow coring of this package has also been attributed to the Holocene in the

Central and Eastern Basins (Drinia et al., 2014; Sakellariou et al., 2007). The attribution of H2 and H3 to ~130 ka and ~325 ka respectively has some dependency on the sill-controlled temporal distribution of lacustrine and marine intervals. These correlations therefore carry some uncertainty although we consider the ~130 and ~325 ka correlations to be most plausible. We stress that although fault slip rates and timings reported here carry uncertainty introduced by these assumptions, the relative timing and order of fault migration events based on horizon offsets can be interpreted independently of this.

Comparing the age model presented in this study to similarly constructed age models for syn-rift sedimentation in the Gulf of Corinth (Figure 1c) based on sill-controlled base-level changes (e.g., Bell et al., 2008; Lykousis et al., 2007b; Nixon et al., 2016) offers some comparative validation of our North Gulf of Evia age model. H1 (~12 ka) and H2 (~130 ka) in our study correlate with the upper two key horizons (H1 and H2) in the Gulf of Corinth correlation of Nixon et al. (2016). Horizon H3 from our study has a proposed age of ~325 ka and is equivalent to H4 (~340 ka) in the model of Nixon et al. (2016) with the small age discrepancy likely related to the position within the highstand package that the horizon is mapped.

The efficacy of the seismic age models of Nixon et al. (2016) and others have recently been tested following International Ocean Discovery Program (IODP) drilling in the Gulf of Corinth (McNeill et al., 2026, 2019; Nixon et al., 2024; Pechlivanidou et al., 2025). This drilling has allowed the magneto- and bio-stratigraphic dating of Corinth seismic horizons H1 (13 ka), H2 (129 ka) and H4 (335 ka). The results have shown that the proposed ages from the seismic stratigraphic model to be within 5 ka of the independent dating results (Nixon et al., 2024), which gives us confidence that our approach is robust.

Despite this, differences in sediment routing systems, climate sensitivity, and depocenter geometries have resulted in disparities in the seismic expression of syn-rift units between the two rift systems that impact the comparative application of the age model across the gulfs. Seismic units in the deep basin settings in Corinth alternate between thick low amplitude packages, correlated to lowstand lacustrine deposition, and thin high amplitude packages correlated to marine deposition during highstands (Bell et al., 2008; Nixon et al., 2024). In contrast, the late-Pleistocene seismic units in the North Gulf of Evia are near-universally characterised by high amplitude reflections (Figure 5 and 6). This reflects the greater sensitivity of the North Gulf of Evia to sea level change due to a combination of the 40 m Lichades Sill to the Aegean Sea (Figure 2b; 20 m shallower than the Rion Sill to the Gulf of Corinth; McNeill et al., 2019) and the overall shallow bathymetry and palaeo-bathymetry of the Western Basin (<120 m; Figure 7). As a result, sedimentation across much of the Western Basin is restricted to interglacial highstands (e.g., MIS 5, 7 and 9) as lowstand Pleistocene glacial lakes (e.g., MIS 2 and 6) were likely confined to the deep Central Basin (Van Andel and Perissoratis, 2006). The distinct periods of subaerial exposure of the Western Basin (Figure 10b) are also not widely seen across the Gulf of Corinth (Gawthorpe et al., 2018).

Reliable sedimentation rates are difficult to constrain in the Western Basin due to the strongly developed H1 and H2 erosive surfaces (Figure 5). We do however infer that sedimentation in the Western Basin is markedly slower than in the main depocenters of the Gulf of Corinth. In the well-preserved seismic packages in the south of Figure 9, where erosion appears to be minimal, sedimentation rates of 0.1-0.3 mm/yr are calculated for the thickest sections of SU3 (20-54 m over ~195 kyrs) and 0.1-0.2 mm/yr (10-20 m over ~120 kyrs) for SU2. Despite these rates likely representing maxima in the Western Basin, they are an order of magnitude slower than sedimentation over comparable time intervals in the main depocenters of the Gulf of Corinth of 1-3 mm/yr (McNeill et al., 2019).

5.3 Normal fault migration in the North Gulf of Evia

In the example of the western North Gulf of Evia, the overall structural anatomy of the rift reflects an asymmetric graben with dominant structural control from the onshore Coastal Faults and near-offshore Kalypso Fault (Figure 10d).

Younging of fault activity towards the Central Graben and Kalypso Fault is resolved (Figure 7a). Faults on the northern margin of the basin have not generated significant accommodation, nor do they show significant slip, during the deposition of SU1-3 with the major depocenters found to the south of the Central Graben (Figure 7b and 8). The Kalypso Fault represents the northernmost migration of the fault systems of the southern margin of the rift while migration from the north has localised on the Central Graben (Figure 6b). Holocene slip in the Central Graben is significant with ~2 mm/yr slip on the north-dipping structure and ~1 mm/yr slip on the south-dipping fault. The south-dipping fault generated significant hanging wall accommodation prior to ~325 ka (Figure 7d and 8).

Faults on the northern margin of the western basin appear to have migrated to broadly parallel structures (Figure 7a). In contrast, the main migration event on the southern margin from the Arkitsa Fault to Kalypso Fault has occurred across non-parallel faults with evolving strike (Arkitsa = ~280°; Kalypso = ~260°; Figure 10d). This is interpreted to reflect the geodynamic rotational influence on fault migration in the gulf. The western tip of both Arkitsa and Kalypso segments join the Agios Konstantinos Fault at the same point resulting in extremely tight fault spacing in this area (Figure 10d). It appears that this western tip has acted as a rotational axis for this migration event after block rotation has modified the strike of the Arkitsa Fault to be less favourable to slip under the prevailing stress regime (c.f., Jackson, 1999). Theoretical mechanical models suggest that after a threshold block rotation of 20-40° is met, the active front of deformation must relocalize to newly formed, optimallyoriented fault (Nur et al., 1986). The ~20° evolution of strike between the Arkitsa and Kalypso Faults falls within the expected range of this mechanical threshold.

The strike of the Kalypso Fault also reflects a comparable extension azimuth to the ~70° strike rupture plane resolved for the 2013 Mw = 5.4 Kallidromon earthquake sequence in the same tectonic system (Ganas et al., 2014). This is consistent with measured strain from geodetic studies which show present extension acts at an azimuth of ~0 - 10° (Briole et al., 2021; Chousianitis et al., 2024; Sboras et al., 2025). This suggests that faults oriented similarly to the Kalypso Fault represent a pervasive active structural fabric across the western rift system.

Activity on the Kalypso Fault initiated at ~325 ka, as inferred from a reverse in thickening direction at this time towards the structure (Figure 8 and 9). The uplifted marine terrace staircase in the footwall of the structure (Figure 10; Papanastassiou et al., 2014) implies that footwall uplift of the Kalypso Fault has exceeded hanging wall subsidence of the Arkitsa Fault over the late-Pleistocene. To achieve this, the Kalypso Fault has likely undergone fault linkage to the other segments of the Coastal Fault System. This implies that the Arkitsa Fault has seen a marked reduction in slip rate since the initiation of the Kalypso, in agreement with previous work where late-Pleistocene slip on the Arkitsa Fault is reported to be as low as 0.7 mm/yr (Walker et al., 2010; Whittaker and Walker, 2015).

Although all of the offshore faults mapped in this study have at least some normal slip component (Figure 7), the existence of oblique- and strike-slip structures across the North Gulf of Evia domain (Figure 2a; e.g., Faucher et al., 2021; Ganas et al., 2016; Kranis et al., 2001; Palyvos et al., 2006) suggests that non-dip-slip deformation in the Western Basin is likely. Resolving this oblique component, however, represents a limitation of current offshore datasets due to the 100s m to km-scale spacing between 2D seismic profiles (Figure 2b).

However, the small flower structures resolved in Figure 9 and spatial variability in SU2-3 depocenters in Figure 8 provide some evidence for active, rift axial strike-slip deformation in the Western Basin. This is consistent with the rift-axial, left-lateral strike-slip Melouna Fault in the Eastern Basin of the gulf deduced from earthquake focal mechanisms (Figure 2a; Ganas et al., 2016).

The Kalypso Fault has a segment length of ~12 km (Figure 7) and a linked length of ~30 km to the Kammena Vourla Fault segment (Figure 2b). Our resolved throw rate of ~3.75 mm/yr corresponds to a slip rate of ~4.0-4.3 mm/yr assuming fault dip of 60-70° and is consistent with the large normal fault (>10 km length) displacement-length scaling relationships of Lathrop et al. (2022) given an initiation age of 325 ka. The Kalypso Fault presents significant regional seismic hazard and is capable of hosting Mw > 6 earthquakes (Wells and Coppersmith, 1994) and given its offshore location, also presents significant tsunami hazard to the North Gulf of Evia. The Kalypso Fault could provide a potential source for the currently unattributed tsunami-forming earthquake of 426 BCE (Freitag and Reicherter, 2019).

The establishment of the Kalypso Fault to become the dominant structural control on the western rift occurred rapidly with significant throw accumulation and lateral growth occurring within ~325 kyrs. This highlights the rapid onset of slip on the Kalypso Fault to become dominant over timescales less than 100 kyrs, likely close to 10 kyrs, and implies that normal fault migration and establishment in young rift systems occur rapidly over these timescales.

5.4 Implications for complex rift systems

Complex and composite geodynamic settings are common in active rift systems (e.g., Brune et al., 2023; Laó-Dávila et al., 2015; Mouslopoulou et al., 2007; Saria et al., 2014; Wallace et al., 2004) and rifts preserved in the geological record (e.g., Duffy et al., 2015; Frizon de Lamotte et al., 2015). Here we aim to contextualize the structural complexity of the North Gulf of Evia through comparison to other orthogonal and complex rift systems.

First, comparing the structure and evolution of the western North Gulf of Evia to the Gulf of Corinth highlights some key contrasts despite the rifts accommodating the same extensional stress regime (Figure 1b-c; Chousianitis et al., 2024). Most notably, normal fault zones in the Gulf of Corinth, have migrated basin-ward to sub-parallel structures, approximately orthogonal to the orientation of principal extension (Figure 1c; Ford et al., 2017; Nixon et al., 2024). This contrasts the North Gulf of Evia where we resolve rotational fault migration between the Arkitsa and Kalypso Faults and map major faults that strike obliquely to the principal extension orientation (e.g., Central Graben; Figure 8).

The Gulf of Corinth rift is also not segmented by oblique- and strike-slip fault belts (Figure 1c) which are well developed in the North Gulf of Evia (Figure 1b; Kranis et al., 2001; Palyvos et al., 2006). As a result, major sedimentary depocenters in the Gulf of Corinth have developed at the centre of linked fault zones (Nixon et al., 2016) while in the Western Basin of the North Gulf of Evia, the main late-Pleistocene depocenters are located at the eastern tip of the major linked fault zone of the rift, the Coastal Fault System (Whittaker and Walker, 2015), and are instead located in the hanging wall of the Kalypso Fault (Figure 8a-c).

The Lake Malawi Rift provides a comparative example in an oblique rift setting with a similar level of climatic sensitivity to the North Gulf of Evia (Lyons et al., 2011). Although the Malawi Rift is considered to be at more mature stage of rifting, major normal faults are also found to have non-parallel strike and marked shifts in the polarity of rift asymmetry are resolved along the length of the rift (Laó-Dávila et al., 2015; Scholz et al., 2020). Rift-oblique fault belts are similarly found to segment the rift here and these introduce asymmetric distributions of syn-rift depocenters (Laó-Dávila et al., 2015; Scholz et al., 2020).

The fault geometries produced by rotational rifting in the Taupo Rift, New Zealand (Schmid et al., 2022; Seebeck et al., 2014) share similarities to the Western North Gulf of Evia. The Taupo Rift widens from southwest, closest to the rotational axis, to the northeast with a V-shaped fault geometry and is associated with strike- and oblique-slip structures parallel to the rift axis (Mouslopoulou et al., 2007; Seebeck et al., 2014). This is comparable to the widening of fault activity in the offshore Western Basin from west to east resolved in this study (Figure 7) and the oblique-slip inferred for the rift-axial fault zone in Figure 9. Similarly, the bounding faults of the Central Graben produce a V-shaped geometry (Figure 7), strongly characteristic of rotational rifting (Schmid et al., 2022; Zwaan et al., 2020b).

Analogue and numerical models are commonly used explore the influence of rotational strain on rift development (e.g., Duclaux et al., 2020; Molnar et al., 2017; Schmid et al., 2022; Zwaan et al., 2020; Zwaan and Schreurs, 2020) yet natural records of normal fault processes in these settings remain underexamined. Processes such as the oblique fault migration and rapid slip accumulation resolved here on the Kalypso Fault are likely not unique to the North Gulf of Evia and occur across many active and failed rift systems such as those outlined above. Evaluating these processes in the North Gulf of Evia and exploring the impact of propagating strike-slip deformation on rift segmentation and evolution remain active research challenges (e.g., Caroir et al., 2024; Sboras et al., 2025) that we hope the development of the joint stratigraphic and structural framework outlined here can contribute towards. The addition of new studies such as this, with strong temporal constraints in natural, complex rift settings will help us to further develop a detailed understanding of how faults and fault systems grow and migrate rapidly and interact in non-simple tectonic regimes. In turn, this will serve to improve the accuracy and applicability of numerical and analogue models of rift processes.

6 Conclusions

This study provides a high-resolution record of normal fault migration and basin evolution during complex rifting from the western North Gulf of Evia, Central Greece. Here extension is influenced by continental block rotation and strike-slip deformation from the North Anatolian Fault (Figure 1a and 2) and as such, the rift offers a structural contrast to the nearby orthogonal rifting in the Gulf of Corinth, while similarities to the oblique rifting in Lake Malawi and the rotational Taupo Rift are resolved.

In this work:

- A consistent, syn-kinematic, seismic stratigraphic age model for the North Gulf of Evia is defined for the first time, with three key mappable surfaces (H1-3) attributed ages of ~12, ~130 and ~325 ka, based on a base-level correlation to subsurface clinoform packages.
- Major syn-rift depocentres are found to be located along the southern margin of the basin in the hanging wall of the Kalypso Fault (~4 mm/yr slip rate) and additional significant syn-kinematic control from the axial Central Graben (~1 – 2 mm/yr slip) is observed.
- Basinward migration of the active front of normal faulting is observed on both margins of the rift system over the 10-100s kyr timescales resolved in this study. Faults on the northern margin have migrated to sub-parallel structures (e.g., Central Graben) while fault migration on the southern margin has occurred between structures with evolving strike of ~20° (e.g., Kalypso Fault).

- The Kalypso Fault is found to exert dominant structural control on the basin currently. This initiated at ~325 ka following an oblique fault migration event from the onshore Arkitsa Fault. The Kalypso Fault established rapidly as the dominant fault over timescales of 10s kyrs and is linked to the existing, onshore Coastal Fault System.

This study demonstrates the value of temporal constraints on syn-kinematic sedimentation derived from high-resolution subsurface data to examine rapidly evolving fault and fault system processes in complex settings.

Data Availability

The fault network produced from this study is available as a .kml file. Uninterpreted seismic profiles presented in this study are available in the Supplementary Materials. Seismic reflection data is available on request.

References

Agostini, A., Corti, G., Zeoli, A., Mulugeta, G., 2009. Evolution, pattern, and partitioning of deformation during oblique continental rifting: Inferences from lithospheric-scale centrifuge models. Geochemistry, Geophysics, Geosystems 10. https://doi.org/10.1029/2009GC002676

Armijo, R., Meyer, B., King, G.C.P., Rigo, A., Papanastassiou, D., 1996. Quaternary evolution of the Corinth Rift and its implications for the Late Cenozoic evolution of the Aegean. Geophysical Journal International 126, 11–53. https://doi.org/10.1111/j.1365-246X.1996.tb05264.x

Bell, R.E., Duclaux, G., Nixon, C.W., Gawthorpe, R.L., McNeill, L.C., 2017. High-angle, not low-angle, normal faults dominate early rift extension in the Corinth Rift, central Greece. Geology 46, 115–118. https://doi.org/10.1130/G39560.1

Bell, R.E., McNeill, L.C., Bull, J.M., Henstock, T.J., 2008. Evolution of the offshore western Gulf of Corinth. GSA Bulletin 120, 156–178. https://doi.org/10.1130/B26212.1

Bell, R.E., McNeill, L.C., Bull, J.M., Henstock, T.J., Collier, R.E.L., Leeder, M.R., 2009. Fault architecture, basin structure and evolution of the Gulf of Corinth Rift, central Greece. Basin Research 21, 824–855. https://doi.org/10.1111/j.1365-2117.2009.00401.x

Bradley, K.E., Vassilakis, E., Hosa, A., Weiss, B.P., 2013. Segmentation of the Hellenides recorded by Pliocene initiation of clockwise block rotation in Central Greece. Earth and Planetary Science Letters 362, 6–19. https://doi.org/10.1016/j.epsl.2012.11.043

Briole, P., Ganas, A., Elias, P., Dimitrov, D., 2021. The GPS velocity field of the Aegean. New observations, contribution of the earthquakes, crustal blocks model. Geophysical Journal International 226, 468–492. https://doi.org/10.1093/gji/ggab089

Brune, S., 2014. Evolution of stress and fault patterns in oblique rift systems: 3-D numerical lithospheric-scale experiments from rift to breakup. Geochemistry, Geophysics, Geosystems 15, 3392–3415. https://doi.org/10.1002/2014GC005446

Brune, S., Corti, G., Ranalli, G., 2017. Controls of inherited lithospheric heterogeneity on rift linkage: Numerical and analog models of interaction between the Kenyan and Ethiopian rifts across the Turkana depression. Tectonics 36, 1767–1786. https://doi.org/10.1002/2017TC004739

Brune, S., Kolawole, F., Olive, J.-A., Stamps, D.S., Buck, W.R., Buiter, S.J.H., Furman, T., Shillington, D.J., 2023. Geodynamics of continental rift initiation and evolution. Nature Reviews Earth & Environment 4, 235–253. https://doi.org/10.1038/s43017-023-00391-3

Caroir, F., Chanier, F., Gaullier, V., Sakellariou, D., Bailleul, J., Maillard, A., Paquet, F., Watremez, L., Averbuch, O., Graveleau, F., Ferrière, J., 2024. Late Quaternary deformation in the western extension of the North Anatolian Fault (North Evia, Greece): Insights from very high-resolution seismic data (WATER surveys). Tectonophysics 870, 230138–230138. https://doi.org/10.1016/j.tecto.2023.230138

Catuneanu, O., 2002. Sequence stratigraphy of clastic systems: concepts, merits, and pitfalls. Journal of African Earth Sciences 35, 1–43. https://doi.org/10.1016/S0899-5362(02)00004-0

Chandresh, R., Whittaker, A.C., Bell, R.E., Corti, G., Tortelli, G., Rosa, A.L., Pagli, C., Sani, F., Keir, D., 2026. Spatial and Temporal Evolution of Graben Formation During Rift Linkage Using Quantitative Geomorphology: Insights From Central Afar. Tectonics 45, e2025TC009276. https://doi.org/10.1029/2025TC009276

Chanier, F., Gaullier, V., 2017. WATER cruise, Téthys II R/V, Sismer. https://doi.org/10.17600/17009400

Chanier, F., Watremez, L., 2021. WATER 2 cruise, RV Téthys II. https://doi.org/doi.org/10.17600/18001115

Chousianitis, K., Sboras, S., Mouslopoulou, V., Chouliaras, G., Hristopulos, D.T., 2024. The Upper Crustal Deformation Field of Greece Inferred From GPS Data and Its Correlation With Earthquake Occurrence. Journal of Geophysical Research: Solid Earth 129, e2023JB028004. https://doi.org/10.1029/2023JB028004

Coveney, S.M., Bell, R.E., Wils, K., Lastras, G., Whittaker, A.C., 2025. The Early Evolution of a Young Normal Fault in the Aysén Fjord, Chile. Tectonics 44, e2025TC008835. https://doi.org/10.1029/2025TC008835

Cowie, P.A., Attal, M., Tucker, G.E., Whittaker, A.C., Naylor, M., Ganas, A., Roberts, G.P., 2006. Investigating the surface process response to fault interaction and linkage using a numerical modelling approach. Basin Research 18, 231–266. https://doi.org/10.1111/j.1365-2117.2006.00298.x

Cundy, A.B., Gaki-Papanastassiou, K., Papanastassiou, D., Maroukian, H., Frogley, M.R., Cane, T., 2010. Geological and geomorphological evidence of recent coastal uplift along a major Hellenic normal fault system (the Kamena Vourla fault zone, NW Evoikos Gulf, Greece). Marine Geology 271, 156–164. https://doi.org/10.1016/j.margeo.2010.02.009

de Gelder, G., Fernández-Blanco, D., Melnick, D., Duclaux, G., Bell, R.E., Jara-Muñoz, J., Armijo, R., Lacassin, R., 2019. Lithospheric flexure and rheology determined by climate cycle markers in the Corinth Rift. Sci Rep 9, 4260. https://doi.org/10.1038/s41598-018-36377-1

Drinia, H., Antonarakou, A., Anastasakis, G., 2014. Late Quaternary micropalaeontological record of a semi-enclosed marine basin, North Evoikos, central Aegean Sea. Quaternary International 345, 18–31. https://doi.org/10.1016/j.quaint.2014.04.011

Duclaux, G., Huismans, R.S., May, D.A., 2020. Rotation, narrowing, and preferential reactivation of brittle structures during oblique rifting. Earth and Planetary Science Letters 531, 115952. https://doi.org/10.1016/j.epsl.2019.115952

Duffy, O.B., Bell, R.E., Jackson, C.A.-L., Gawthorpe, R.L., Whipp, P.S., 2015. Fault growth and interactions in a multiphase rift fault network: Horda Platform, Norwegian North Sea. Journal of Structural Geology 80, 99–119. https://doi.org/10.1016/j.jsg.2015.08.015

EMODnet, 2022. EMODnet Digital Bathymetry (DTM 2022). https://doi.org/10.12770/ff3aff8a-cff1-44a3-a2c8-1910bf109f85

Faucher, A., Gueydan, F., Jolivet, M., Alsaif, M., Célérier, B., 2021. Dextral Strike-Slip and Normal Faulting During Middle Miocene Back-Arc Extension and Westward Anatolia Extrusion in Central Greece. Tectonics 40, e2020TC006615. https://doi.org/10.1029/2020TC006615

Feng, Y., Jiang, S., Hu, S., Li, S., Lin, C., Xie, X., 2016. Sequence stratigraphy and importance of syndepositional structural slope-break for architecture of Paleogene syn-rift lacustrine strata, Bohai Bay Basin, E. China. Marine and Petroleum Geology 69, 183–204. https://doi.org/10.1016/j.marpetgeo.2015.10.013

Fernández-Blanco, D., de Gelder, G., Lacassin, R., Armijo, R., 2019. A new crustal fault formed the modern Corinth Rift. Earth-Science Reviews 199, 102919. https://doi.org/10.1016/j.earscirev.2019.102919

Ford, M., Hemelsdaël, R., Mancini, M., Palyvos, N., 2017. Rift migration and lateral propagation: evolution of normal faults and sediment-routing systems of the western Corinth rift (Greece). Geological Society, London, Special Publications 439, 131–168. https://doi.org/10.1144/SP439.15

Freitag, K., Reicherter, K., 2019. The earthquake and tsunami of 426 BC in Greece: observations by Thucydides and contextual interpretations. Zeitschrift für Geomorphologie, Supplementary Issues 62, 47–62. https://doi.org/10.1127/zfg_suppl/2019/0625

Frizon de Lamotte, D., Fourdan, B., Leleu, S., Leparmentier, F., de Clarens, P., 2015. Style of rifting and the stages of Pangea breakup. Tectonics 34, 1009–1029. https://doi.org/10.1002/2014TC003760

Galanakis, D., Sboras, S., Sakellariou, D., Pavlides, S., Iordanidou, K., Georgiou, C., Ganas, A., Koukouvelas, I., Kranis, C., Lalechos, S., Rondoyanni, T., Lekkas, E., 2025. The Hellenic DataBase of Active Faults (HeDBAF): a new, national geodatabase of active faults for the broader Greek territory. Presented at the EGU 2025, Copernicus Meetings, Vienna. https://doi.org/10.5194/egusphere-egu25-9230

Ganas, A., Karastathis, V., Moshou, A., Valkaniotis, S., Mouzakiotis, E., Papathanassiou, G., 2014. Aftershock relocation and frequency–size distribution, stress inversion and seismotectonic setting of the 7 August 2013 M=5.4 earthquake in Kallidromon Mountain, central Greece. Tectonophysics 617, 101–113. https://doi.org/10.1016/j.tecto.2014.01.022

Ganas, A., Mouzakiotis, E., Moshou, A., Karastathis, V., 2016. Left-lateral shear inside the North Gulf of Evia Rift, Central Greece, evidenced by relocated earthquake sequences and moment tensor inversion. Tectonophysics 682, 237–248. https://doi.org/10.1016/j.tecto.2016.05.031

Ganas, A., Oikonomou, I.A., Tsimi, C., 2013. NOAfaults: a digital database for active faults in Greece. Bulletin of the Geological Society of Greece 47, 518–530. https://doi.org/10.12681/bgsg.11079

Ganas, A., Roberts, G.P., Memou, T., 1998. Segment boundaries, the 1894 ruptures and strain patterns along the Atalanti Fault, Central Greece. Journal of Geodynamics 26, 461–486. https://doi.org/10.1016/S0264-3707(97)00066-5

Gawthorpe, R.L., Andrews, J.E., Collier, R.E.L., Ford, M., Henstra, G.A., Kranis, H., Leeder, M.R., Muravchik, M., Skourtsos, E., 2017. Building up or out? Disparate sequence architectures along an active rift margin—Corinth rift, Greece. Geology 45, 1111–1114. https://doi.org/10.1130/G39660.1

Gawthorpe, R.L., Leeder, M.R., 2000. Tectono-sedimentary evolution of active extensional basins. Basin Research 12, 195–218. https://doi.org/10.1111/j.1365-2117.2000.00121.x

Gawthorpe, R.L., Leeder, M.R., Kranis, H., Skourtsos, E., Andrews, J.E., Henstra, G.A., Mack, G.H., Muravchik, M., Turner, J.A., Stamatakis, M., 2018. Tectono-sedimentary evolution of the Plio-Pleistocene Corinth rift, Greece. Basin Research 30, 448–479. https://doi.org/10.1111/bre.12260

Goldsworthy, M., Jackson, J., Haines, J., 2002. The continuity of active fault systems in Greece. Geophysical Journal International 148, 596–618. https://doi.org/10.1046/j.1365-246X.2002.01609.x

Harding, T.P., 1985. Seismic Characteristics and Identification of Negative Flower Structures, Positive Flower Structures, and Positive Structural Inversion1. AAPG Bulletin 69, 582–600. https://doi.org/10.1306/AD462538-16F7-11D7-8645000102C1865D

Hatzfeld, D., Ziazia, M., Kementzetzidou, D., Hatzidimitriou, P., Panagiotopoulos, D., Makropoulos, K., Papadimitriou, P., Deschamps, A., 1999. Microseismicity and focal mechanisms at the western termination of the North Anatolian Fault and their implications for continental tectonics. Geophysical Journal International 137, 891–908. https://doi.org/10.1046/j.1365-246x.1999.00851.x

Huang, L., Liu, C., 2017. Three Types of Flower Structures in a Divergent-Wrench Fault Zone. Journal of Geophysical Research: Solid Earth 122, 10,478-10,497. https://doi.org/10.1002/2017JB014675

IGME, 2006. Geological Map of Greece, 1:50,000 Scale (Pelasgia sheet, 2006; Istaia sheet, 1984; Elatia sheet, 1967; Atalanti sheet, 1965).

Jackson, C., Bell, R.E., Rotevatn, A., Tvedt, A.B.M., 2017. Techniques to determine the kinematics of synsedimentary normal faults and implications for fault growth models, in: Childs, C., Holdsworth, R.E., Jackson, C.A.-L., Manzocchi, T., Walsh, J.J., Yielding, G. (Eds.), The Geometry and Growth of Normal Faults. The Geological Society of London, p. 0. https://doi.org/10.1144/SP439.22

Jackson, J., 1999. Fault death: a perspective from actively deforming regions. Journal of Structural Geology 21, 1003–1010. https://doi.org/10.1016/S0191-8141(99)00013-9

Jolivet, L., Faccenna, C., Huet, B., Labrousse, L., Le Pourhiet, L., Lacombe, O., Lecomte, E., Burov, E., Denèle, Y., Brun, J.-P., Philippon, M., Paul, A., Salaün, G., Karabulut, H., Piromallo, C., Monié, P., Gueydan, F., Okay, A.I., Oberhänsli, R., Pourteau, A., Augier, R., Gadenne, L., Driussi, O., 2013. Aegean tectonics: Strain localisation, slab tearing and trench retreat. Tectonophysics, The Aegean: a natural laboratory for tectonics - Neotectonics 597–598, 1–33. https://doi.org/10.1016/j.tecto.2012.06.011

Jourdon, A., Le Pourhiet, L., Mouthereau, F., May, D., 2020. Modes of Propagation of Continental Breakup and Associated Oblique Rift Structures. Journal of Geophysical Research: Solid Earth 125, e2020JB019906. https://doi.org/10.1029/2020JB019906

Kokkalas, S., Jones, R.R., McCaffrey, K.J.W., Clegg, P., 2007. Quantitative fault analysis at Arkitsa, Central Greece, using Terrestrial Laser- Scanning ("LIDAR"). Bulletin of the Geological Society of Greece 40, 1959–1972. https://doi.org/10.12681/bgsg.17237

Kranis, H., 2007. Neotectonic Basin Evolution in Central-Eastern Mainland Greece: An Overview. Bulletin of the Geological Society of Greece 40, 360–373. https://doi.org/10.12681/bgsg.16621

Kranis, H., Palyvos, N., Livaditis, G., Maroukian, H., 2001. The Hyambolis zone: geomorhological and tectonic evidence of a transverse structure in Lokris (Central Greece). Bulletin of the Geological Society of Greece 34, 251–251. https://doi.org/10.12681/bgsg.17020

Laó-Dávila, D.A., Al-Salmi, H.S., Abdelsalam, M.G., Atekwana, E.A., 2015. Hierarchical segmentation of the Malawi Rift: The influence of inherited lithospheric heterogeneity and kinematics in the evolution of continental rifts. Tectonics 34, 2399–2417. https://doi.org/10.1002/2015TC003953

Lathrop, B.A., Jackson, C. a.-L., Bell, R.E., Rotevatn, A., 2022. Displacement/Length Scaling Relationships for Normal Faults; a Review, Critique, and Revised Compilation. Front. Earth Sci. 10. https://doi.org/10.3389/feart.2022.907543

Lykousis, V., Sakellariou, D., Moretti, I., Kaberi, H., 2007a. Late Quaternary basin evolution of the Gulf of Corinth: Sequence stratigraphy, sedimentation, fault–slip and subsidence rates. Tectonophysics, Deep structure, fault arrays and surface processes within an active graben: The Gulf of Corinth 440, 29–51. https://doi.org/10.1016/j.tecto.2006.11.007

Lykousis, V., Sakellariou, D., Moretti, I., Kaberi, H., 2007b. Late Quaternary basin evolution of the Gulf of Corinth: Sequence stratigraphy, sedimentation, fault–slip and subsidence rates. Tectonophysics 440, 29–51. https://doi.org/10.1016/j.tecto.2006.11.007

Lyons, R.P., Scholz, C.A., Buoniconti, M.R., Martin, M.R., 2011. Late Quaternary stratigraphic analysis of the Lake Malawi Rift, East Africa: An integration of drill-core and seismic-reflection data. Palaeogeography, Palaeoclimatology, Palaeoecology, Southern hemisphere tropical climate over the past 145ka: Results of the Lake Malawi Scientific Drilling Project, East Africa 303, 20–37. https://doi.org/10.1016/j.palaeo.2009.04.014

McNeill, L.C., Collier, R.E.Ll., De Martini, P.M., Pantosti, D., D'Addezio, G., 2005. Recent history of the Eastern Eliki Fault, Gulf of Corinth: geomorphology, palaeoseismology and impact on palaeoenvironments. Geophysical Journal International 161, 154–166. https://doi.org/10.1111/j.1365-246X.2005.02559.x

McNeill, L.C., Shillington, D.J., Ash, J., Carter, G.D.O., Collier, R.E.Ll., Cvetkoska, A., Diz, P., Doan, M.-L., Everest, J.D., Fabregas, N., Fatourou, E., Ford, M., Gawthorpe, R.L., De Gelder, G., Geraga, M., Gillespie, J., Green, S., Hemelsdaël, R., Herrero-Bervera, E., Ismaiel, M., Janikian, L., Johnson, C., Kafetzidou, A., Koukousioura, O., Kouli, K., Le Ber, E., Li, S., Maffione, M., Mahoney, C., Machlus, M.L., Marret, F., Mazzini, I., Michas, G., Miller, C., Nixon, C.W., Oflaz, S.A., Omale, A.P., Panagiotopoulos, K., Parisi, R., Pechlivanidou, S., Phillips, M.P., Sauer, S., Seguin, J., Sergiou, S., Zakharova, N.V., 2026. A high-resolution record of early rift development and tectonic, sedimentary and environmental conditions in an active rift basin: IODP MSP drilling in the Corinth Rift, Greece (Expedition 381). Marine Geology 496, 107750. https://doi.org/10.1016/j.margeo.2026.107750

McNeill, L.C., Shillington, D.J., Carter, G.D.O., Everest, J.D., Gawthorpe, R.L., Miller, C., Phillips, M.P., Collier, R.E.Ll., Cvetkoska, A., De Gelder, G., Diz, P., Doan, M.-L., Ford, M., Geraga, M., Gillespie, J., Hemelsdaël, R., Herrero-Bervera, E., Ismaiel, M., Janikian, L., Kouli, K., Le Ber, E., Li, S., Maffione, M., Mahoney, C., Machlus, M.L., Michas, G., Nixon, C.W., Oflaz, S.A., Omale, A.P., Panagiotopoulos, K., Pechlivanidou, S., Sauer, S., Seguin, J., Sergiou, S., Zakharova, N.V., Green, S., 2019. High-resolution record reveals climate-driven environmental and sedimentary changes in an active rift. Scientific Reports 9, 3116–3116. https://doi.org/10.1038/s41598-019-40022-w

Mildon, Z.K., Diercks, M., Roberts, G.P., Faure Walker, J.P., Ganas, A., Papanikolaou, I., Sakas, V., Robertson, J., Sgambato, C., Mitchell, S., 2024. Transient Aseismic Vertical Deformation Across the Steeply-Dipping Pisia-Skinos Normal Fault (Gulf of Corinth, Greece). Tectonics 43, e2024TC008276-e2024TC008276. https://doi.org/10.1029/2024TC008276

Molnar, N.E., Cruden, A.R., Betts, P.G., 2017. Interactions between propagating rotational rifts and linear rheological heterogeneities: Insights from three-dimensional laboratory experiments. Tectonics 36, 420–443. https://doi.org/10.1002/2016TC004447

Mouslopoulou, V., Nicol, A., Little, T.A., Walsh, J.J., 2007. Displacement transfer between intersecting regional strike-slip and extensional fault systems. Journal of Structural Geology 29, 100–116. https://doi.org/10.1016/j.jsg.2006.08.002

Nixon, C.W., McNeill, L.C., Bull, J.M., Bell, R.E., Gawthorpe, R.L., Henstock, T.J., Christodoulou, D., Ford, M., Taylor, B., Sakellariou, D., Ferentinos, G., Papatheodorou, G., Leeder, M.R., Collier, R.E.L.I., Goodliffe, A.M., Sachpazi, M., Kranis, H., 2016. Rapid spatiotemporal variations in rift structure during development of the Corinth Rift, central Greece. Tectonics 35, 1225–1248. https://doi.org/10.1002/2015TC004026

Nixon, C.W., McNeill, L.C., Gawthorpe, R.L., Shillington, D.J., Michas, G., Bell, R.E., Moyle, A., Ford, M., Zakharova, N.V., Bull, J.M., de Gelder, G., 2024. Increasing fault slip rates within the Corinth Rift, Greece: A rapidly localising active rift fault network. Earth and Planetary Science Letters 636, 118716. https://doi.org/10.1016/j.epsl.2024.118716

Nur, A., Ron, H., Scotti, O., 1986. Fault mechanics and the kinematics of block rotations. Geology 14, 746–749. https://doi.org/10.1130/0091-7613(1986)14%3C746:FMATKO%3E2.0.CO;2

Palyvos, N., Bantekas, I., Kranis, H., 2006. Transverse fault zones of subtle geomorphic signature in northern Evia island (central Greece extensional province): An introduction to the Quaternary Nileas graben. Geomorphology 76, 363–374. https://doi.org/10.1016/j.geomorph.2005.12.002

Pantosti, D., De Martini, P.M., Papanastassiou, D., Lemeille, F., Palyvos, N., Stavrakakis, G., 2004. Paleoseismological Trenching across the Atalanti Fault (Central Greece): Evidence for the Ancestors of the 1894 Earthquake during the Middle Ages and Roman Times. Bulletin of the Seismological Society of America 94, 531–549. https://doi.org/10.1785/0120020207

Papanastassiou, D., Cundy, A.B., Gaki-Papanastassiou, K., Frogley, M.R., Tsanakas, K., Maroukian, H., 2014. The Uplifted Terraces of the Arkitsa Region, NW Evoikos Gulf, Greece: A Result of Combined Tectonic and Volcanic Processes? The Journal of Geology 122, 397–410. https://doi.org/10.1086/676595

Papanikolaou, D., 2021. The Geology of Greece. https://doi.org/10.1007/978-3-030-60731-9

Papanikolaou, D., Royden, L.H., 2007. Disruption of the Hellenic arc: Late Miocene extensional detachment faults and steep Pliocene-Quaternary normal faults—Or what happened at Corinth? Tectonics 26. https://doi.org/10.1029/2006TC002007

Pechlivanidou, S., Cowie, P.A., Hannisdal, B., Whittaker, A.C., Gawthorpe, R.L., Pennos, C., Riiser, O.S., 2018. Source-to-sink analysis in an active extensional setting: Holocene erosion and deposition in the Sperchios rift, central Greece. Basin Research 30, 522–543. https://doi.org/10.1111/bre.12263

Pechlivanidou, S., Muravchik, M., Gawthorpe, R.L., De Gelder, G., Oflaz, A., Collier, R.E.L., Gillespie, J., Machlus, M.L., Maffione, M., Herrero-Bervera, E., Ford, M., Fabregas, N., Sergiou, S., Geraga, M., Phillips, M.P., Brendryen, J., McNeill, L.C., Shillington, D.J., 2025. Data report: age-depth model of the Corinth synrift sequence, Site M0079, IODP Expedition 381. Proceedings of the International Ocean Discovery Program 381. https://doi.org/10.14379/iodp.proc.381.201.2025

Phillips, T.B., Fazlikhani, H., Gawthorpe, R.L., Fossen, H., Jackson, C.A.-L., Bell, R.E., Faleide, J.I., Rotevatn, A., 2019. The Influence of Structural Inheritance and Multiphase Extension on Rift Development, the NorthernNorth Sea. Tectonics 38, 4099–4126. https://doi.org/10.1029/2019TC005756

Pirazzoli, P.A., Stiros, S.C., Arnold, M., Laborel, J., Laborel-Deguen, F., 1999. Late holocene coseismic vertical displacements and tsunami deposits near Kynos, Gulf of Euboea, Central Greece. Physics and Chemistry of the Earth, Part A: Solid Earth and Geodesy 24, 361–367. https://doi.org/10.1016/S1464-1895(99)00042-3

Roberts, G., Ganas, A., 2000. Fault-slip directions in central and southern Greece measured from striated and corrugated fault planes: Comparison with focal mechanism and geodetic data. Journal of Geophysical Research: Solid Earth 105, 23443–23462. https://doi.org/10.1029/1999JB900440

Roberts, G.P., Koukouvelas, I., 1996. Structural and seismological segmentation of the Gulf of Corinth fault system: implications for models of fault growth. Annals of Geophysics 39. https://doi.org/10.4401/ag-3996

Roberts, S., Jackson, J., 1991. Active normal faulting in central Greece: an overview. Geological Society, London, Special Publications 56, 125–142. https://doi.org/10.1144/GSL.SP.1991.056.01.09

Sakellariou, D., Rousakis, G., Kaberi, H., Kapsimalis, V., Georgiou, P., Kanellopoulos, Th., Lykousis, V., 2007. Tectono-Sedimentary Structure and Late Quaternary Evolution Of The North Evia Gulf Basin, Central Greece: Preliminary Results. Bulletin of the Geological Society of Greece 40, 451–462. https://doi.org/10.12681/bgsg.16644

Saria, E., Calais, E., Stamps, D.S., Delvaux, D., Hartnady, C.J.H., 2014. Present-day kinematics of the East African Rift. Journal of Geophysical Research: Solid Earth 119, 3584–3600. https://doi.org/10.1002/2013JB010901

Sboras, S., Mouzakiotis, E., Chousianitis, K., Karastathis, V., Evangelidis, C.P., Lazos, I., Papageorgiou, A., Liakopoulos, S., Iordanidou, K., 2025. Where does the active North Aegean Sea shear stop? Geodynamic and seismotectonic implications from recent strike-slip earthquake occurrences and GPS-based geodetic analysis in Euboea, Phthiotis and Boeotia, Central Greece. Tectonophysics 914, 230917. https://doi.org/10.1016/j.tecto.2025.230917

Schmid, T.C., Schreurs, G., Adam, J., 2022. Characteristics of continental rifting in rotational systems: New findings from spatiotemporal high resolution quantified crustal scale analogue models. Tectonophysics 822, 229174. https://doi.org/10.1016/j.tecto.2021.229174

Scholz, C., Shillington, D.J., Wright, L.J.M., Accardo, N., Gaherty, J.B., Chindandali, P., 2020. Intrarift fault fabric, segmentation, and basin evolution of the Lake Malawi (Nyasa) Rift, East Africa. Geosphere 16, 1293–1311. https://doi.org/10.1130/GES02228.1

Seebeck, H., Nicol, A., Villamor, P., Ristau, J., Pettinga, J., 2014. Structure and kinematics of the Taupo Rift, New Zealand. Tectonics 33, 1178–1199. https://doi.org/10.1002/2014TC003569

Spratt, R.M., Lisiecki, L.E., 2016. A Late Pleistocene sea level stack. Climate of the Past 12, 1079–1092. https://doi.org/10.5194/cp-12-1079-2016

Vail, P.R., Mitchum, R.M., Jr., Thompson, S., III, 1977. Seismic Stratigraphy and Global Changes of Sea Level, Part 4: Global Cycles of Relative Changes of Sea Level, in: Payton, C.E. (Ed.), Seismic Stratigraphy — Applications to Hydrocarbon Exploration. American Association of Petroleum Geologists, p. 0. https://doi.org/10.1306/M26490C6

Van Andel, T.H., Perissoratis, C., 2006. Late Quaternary depositional history of the North Evvoikos Gulf, Aegean Sea, Greece. Marine Geology 232, 157–172. https://doi.org/10.1016/j.margeo.2006.07.004

Villamor, P., Berryman, K.R., Ellis, S.M., Schreurs, G., Wallace, L.M., Leonard, G.S., Langridge, R.M., Ries, W.F., 2017. Rapid Evolution of Subduction-Related Continental Intraarc Rifts: The Taupo Rift, New Zealand. Tectonics 36, 2250–2272. https://doi.org/10.1002/2017TC004715

Walker, R.T., Claisse, S., Telfer, M., Nissen, E., England, P., Bryant, C., Bailey, R., 2010. Preliminary estimate of Holocene slip rate on active normal faults bounding the southern coast of the Gulf of Evia, central Greece. Geosphere 6, 583–593. https://doi.org/10.1130/GES00542.1

Wallace, L.M., Beavan, J., McCaffrey, R., Darby, D., 2004. Subduction zone coupling and tectonic block rotations in the North Island, New Zealand. Journal of Geophysical Research: Solid Earth 109. https://doi.org/10.1029/2004JB003241

Watkins, S.E., Whittaker, A.C., Bell, R.E., McNeill, L.C., Gawthorpe, R.L., Brooke, S.A.S., Nixon, C.W., 2018. Are landscapes buffered to high-frequency climate change? A comparison of sediment fluxes and depositional volumes in the Corinth Rift, central Greece, over the past 130 k.y. GSA Bulletin 131, 372–388. https://doi.org/10.1130/B31953.1

Wells, D.L., Coppersmith, K.J., 1994. New empirical relationships among magnitude, rupture length, rupture width, rupture area, and surface displacement. Bulletin of the Seismological Society of America 84, 974–1002. https://doi.org/10.1785/BSSA0840040974

Whittaker, A.C., Walker, A.S., 2015. Geomorphic constraints on fault throw rates and linkage times: Examples from the Northern Gulf of Evia, Greece. Journal of Geophysical Research: Earth Surface 120, 137–158. https://doi.org/10.1002/2014JF003318

Wood, J., Whittaker, A.C., Bell, R.E., Coveney, S.M., Kranis, H.D., 2025. Resolving Coseismic and Aseismic Normal Fault Slip Behaviors From InSAR Time Series of the European Ground Motion Service (EGMS). Tectonics 44, e2025TC008904. https://doi.org/10.1029/2025TC008904

Xu, G., Haq, B.U., 2022. Seismic facies analysis: Past, present and future. Earth-Science Reviews 224, 103876. https://doi.org/10.1016/j.earscirev.2021.103876

Yilmaz, Ö., Özer, Z., Beşevli, D.T., Wu, J.E.L., Özsoy, C., Sevinç, S., Bakioglu, K.B., Ercengiz, M.B., Şahin, Ö.K., Dadak, B., Hastürk, T., Yapar, Ö., Dalabasmaz, H., Sipahioglu, N.Ö., Demirci, C., Temel, R.Ö., Akalın, M.F., Sadioglu, M.S.B., 2025. 3-D seismic delineation of the North Anatolian Fault System shear zone in the Western Half of Marmara Basin, Türkiye. Tectonophysics 905, 230726. https://doi.org/10.1016/j.tecto.2025.230726

Zwaan, F., Corti, G., Keir, D., Muluneh, A.A., Illsley-Kemp, F., Papini, M., 2020a. Structural Analysis of the Western Afar Margin, East Africa: Evidence for Multiphase Rotational Rifting. Tectonics 39, e2019TC006043. https://doi.org/10.1029/2019TC006043

Zwaan, F., Schreurs, G., 2020. Rift segment interaction in orthogonal and rotational extension experiments: Implications for the large-scale development of rift systems. Journal of Structural Geology 140, 104119. https://doi.org/10.1016/j.jsg.2020.104119

Zwaan, F., Schreurs, G., Rosenau, M., 2020b. Rift propagation in rotational versus orthogonal extension: Insights from 4D analogue models. Journal of Structural Geology 135, 103946. https://doi.org/10.1016/j.jsg.2019.103946

Figures & Captions:

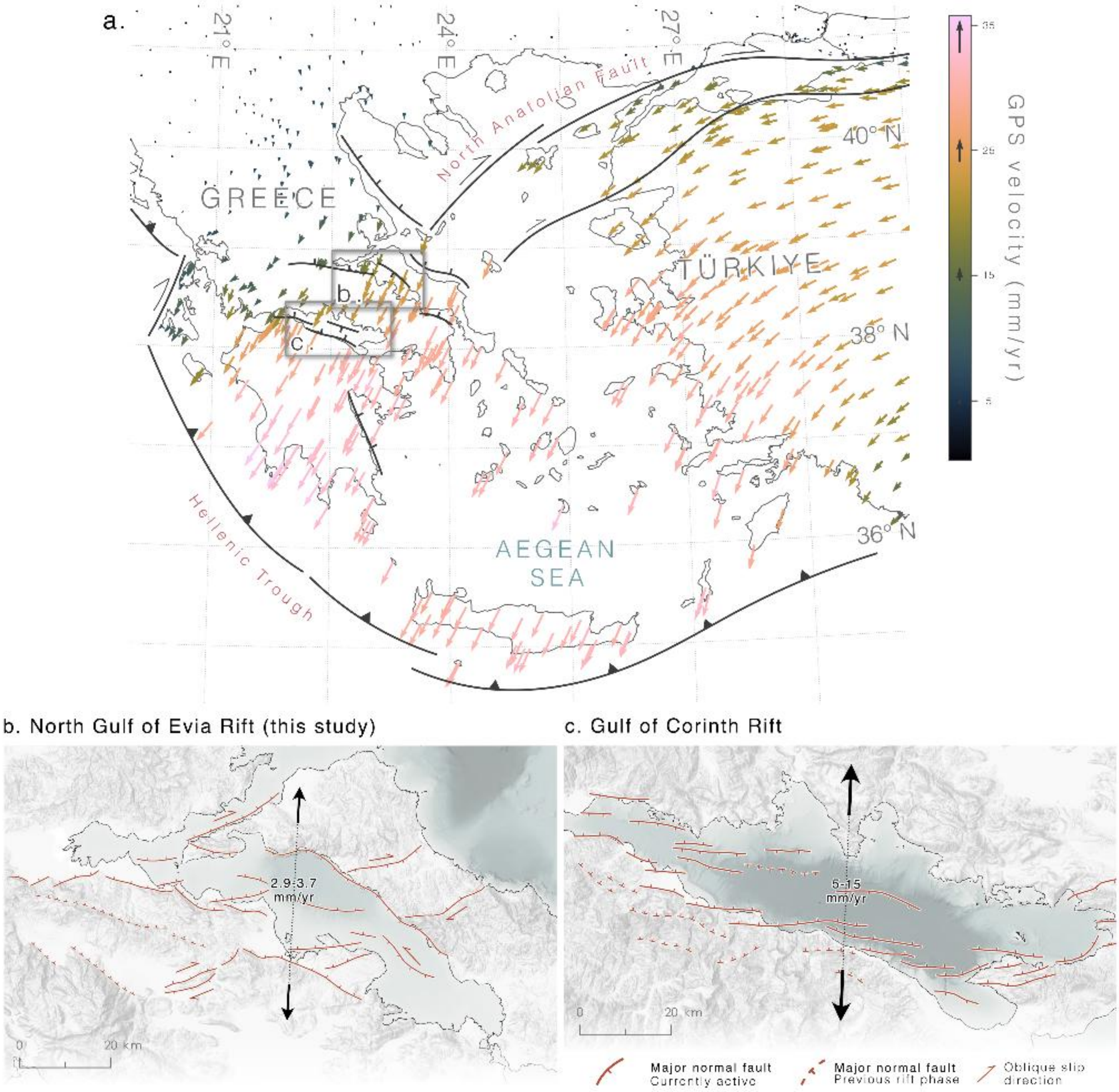

Figure 1: a) Tectonic overview of the Aegean domain with GPS velocity field of the Eastern Mediterranean relative to stable Eurasia from Chousianitis et al. (2024). Major fault zones after (Papanikolaou and Royden, 2007). b and c) Major, rift-scale normal and oblique fault zones of the North Gulf of Evia (b) and Gulf of Corinth (c) rift systems. Black arrows show azimuth of principal extension from Chousianitis et al. (2024). Simplified fault geometries

after a number of studies (Caroir et al., 2024; Kranis, 2007; Nixon et al., 2024; Palyvos et al., 2006). Bathymetry from (EMODnet, 2022).

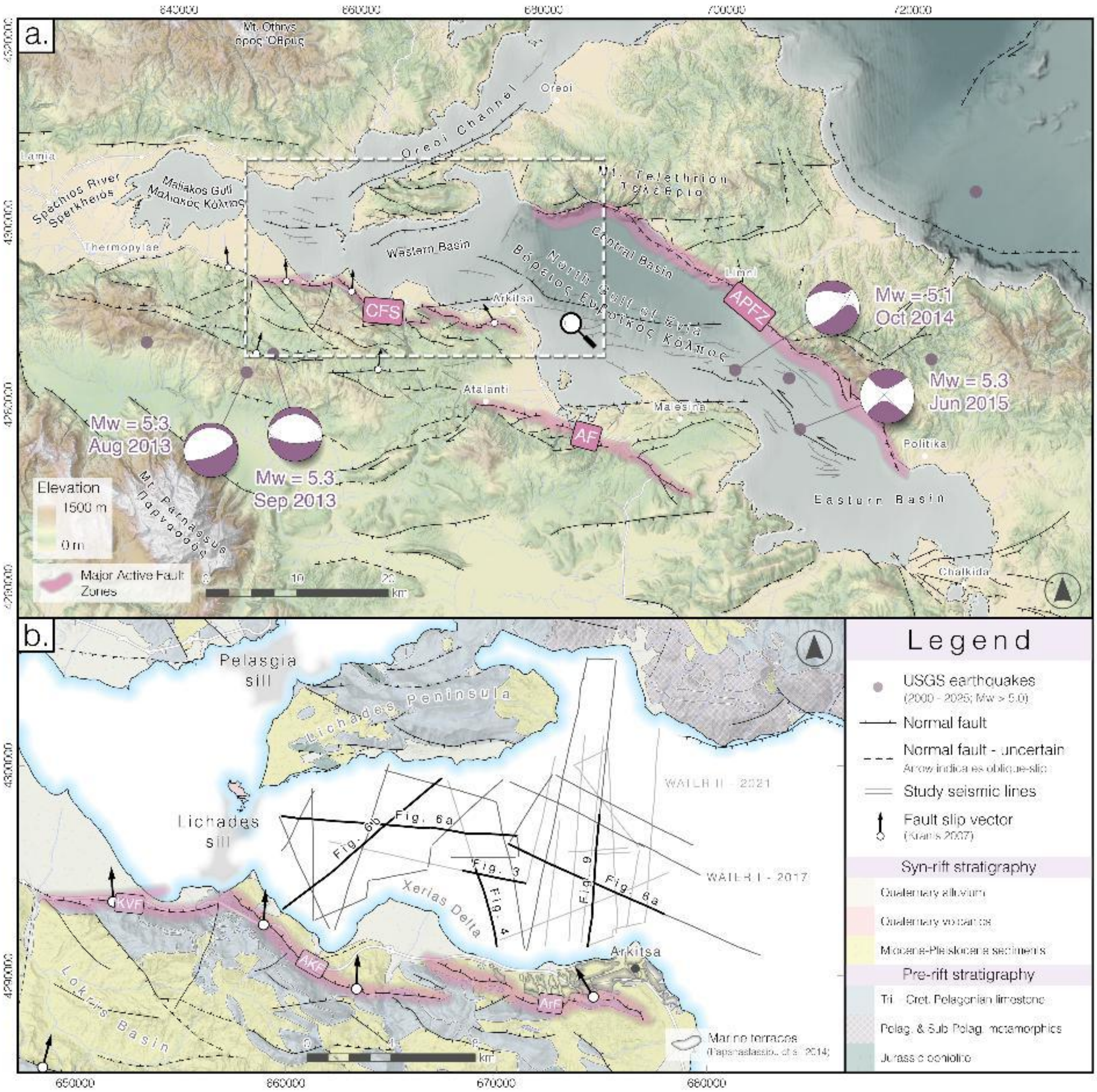

Figure 2: a) Regional tectonic map of the North Gulf of Evia, Central Greece. Major active normal fault zones highlighted in purple. Moment tensors of recent Mw > 5 earthquakes from the USGS database (https://earthquake.usgs.gov/earthquakes/search/). CFS = Coastal Fault System, AF = Atalanti Fault, APFZ = Aedipsos-Politika Fault Zone. Onshore fault traces compiled from a number of studies and databases (Galanakis et al., 2025; Ganas et al., 2013; Kranis, 2007) and primary field study. Offshore faults from Caroir et al., (2024). c) Bedrock

geology of the Western Basin of the North Gulf of Evia (after IGME, 2006) and offshore seismic reflection data profiles used in this study (see Supplementary Figure S5 for profile numbers). Fault slip vectors after Kranis (2007) and Arkitsa terrace outlines after Papanastassiou et al. (2014). KVF = Kammena Vourla Fault, AKF = Agios Konstantinos Fault, ArF = Arkitsa Fault.

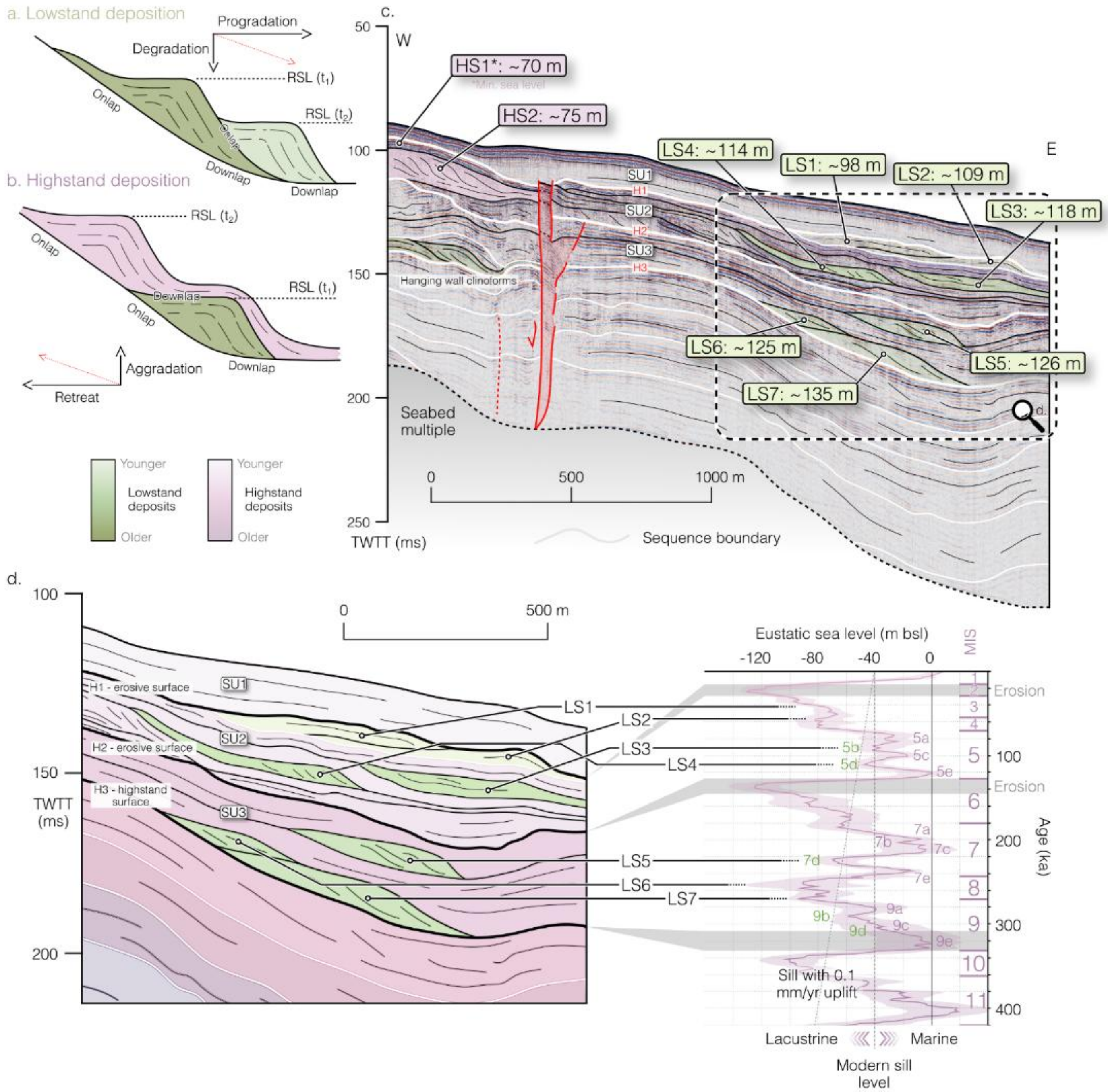

Figure 3: Schematic cartoons showing clinoform package geometries on a basin slope generated following a fall in relative sea level (RSL) from t_1 to t_2 to generate lowstand packages (a) and a rise in RSL (b) to generate highstand packages. Modified based on Catuneanu (2002). c. Seismic interpretation of Line 107 (WATER II) showing 7 identified lowstand packages and 2 marked highstand intervals. Clinoform packages shaded based on highstand or lowstand attribution. Indicated depths are the rollover point of the clinoform package (i.e. base level indicator) based on seismic velocities of 1500 m/s and 1800 m/s for

seawater and sediment respectively. Lowstand sequences are only considered for the age model in the footwall of the minor normal fault zone in the west of the seismic line. d. Detailed view of lowstand package interpretation with correlation to eustatic sea level curve of Spratt and Lisiecki (2016). See Supplementary Figure S6 for uninterpreted seismic section.

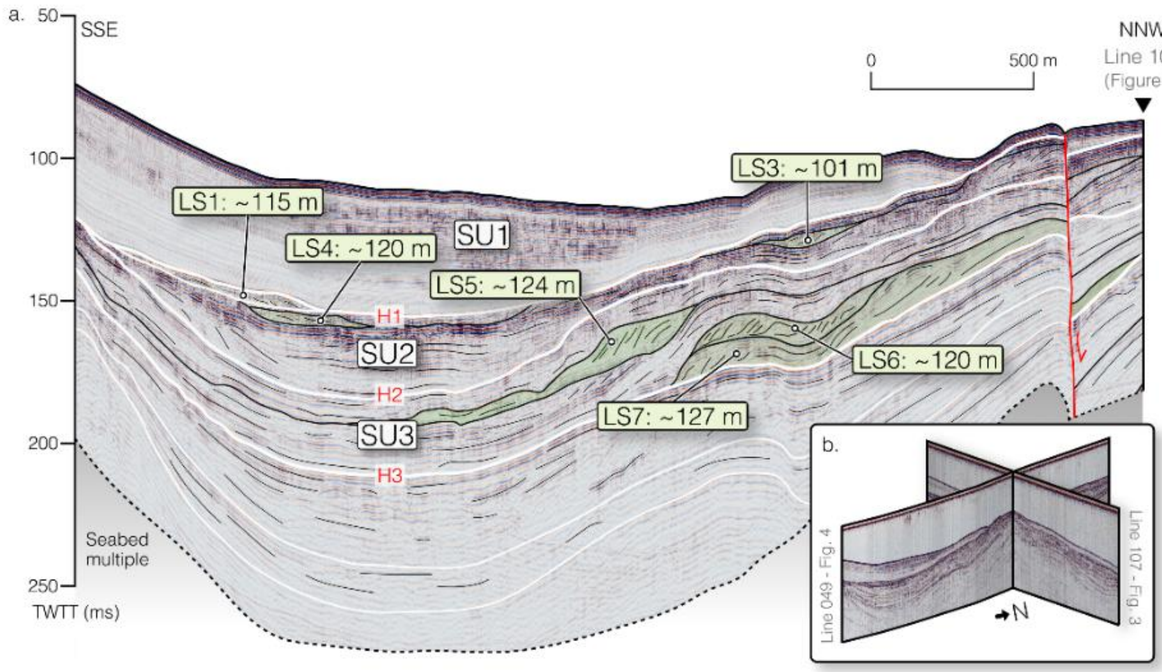

Figure 4: Seismic interpretation of Line 049 (WATER II) with the application of the sequence stratigraphic framework defined in the adjacent line (107) of Figure 3. Marked depths correspond to rollover point of clinoform package. b. 3D model showing the geometric interaction between Line 107 (Figure 2) and Line 049 shown in a. See Supplementary Figure S7 for uninterpreted seismic section.

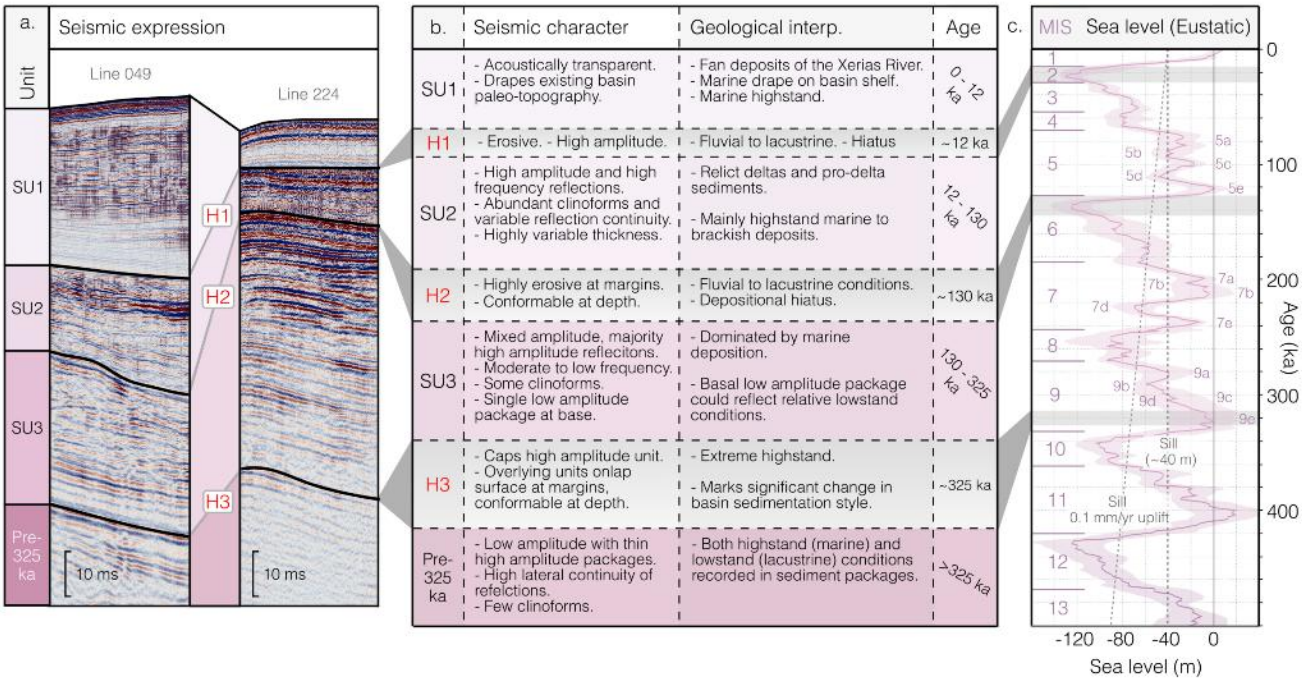

Figure 5: a. Seismic expression of upper syn-rift stratigraphy including seismic horizons (H1-3) and seismic units (SU1-3). b. Description of seismic character of each unit and horizon, geological interpretation of each unit and horizon and age attributed to each unit and horizon based on correlation to the eustatic sea level curve of Spratt and Lisiecki (2016) shown in c. Further seismic examples of mapped surfaces can be found in Supplementary Figure S2.

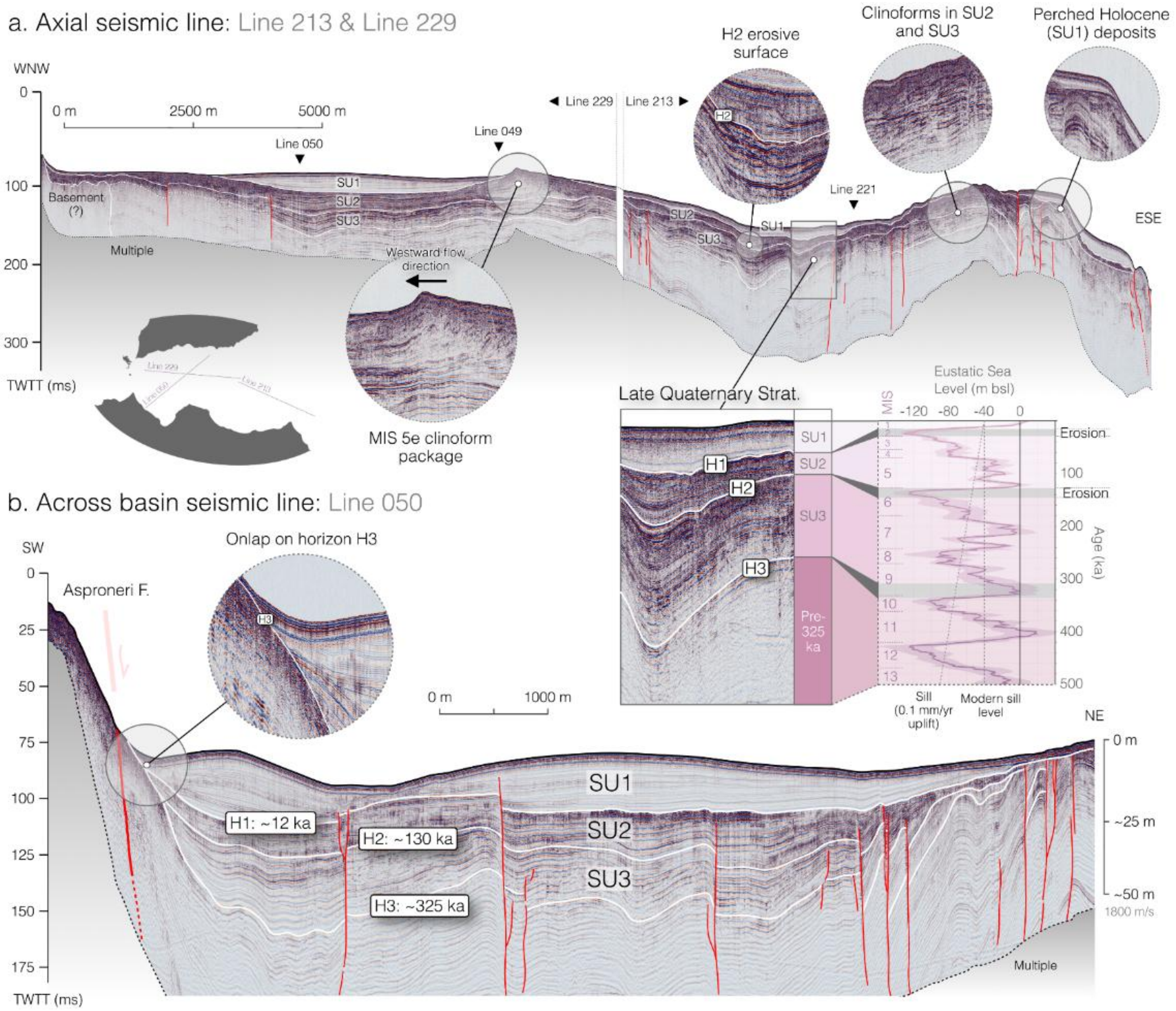

Figure 6: a) Axial seismic reflection profile along the Western Basin (Lines 213 and 229) showing typical seismic sedimentary character, clinoform packages, variable Holocene deposit styles, and major depocenter locations. Stratigraphic age correlation (Figure 3) shown as inset with sea level from Spratt and Lisiecki (2016). b) Across-basin seismic reflection profile (Line 050) showing basin structure including Aspronerì Fault and high fault density in NE. See Supplementary Figure S8 and S9 for uninterpreted seismic sections.

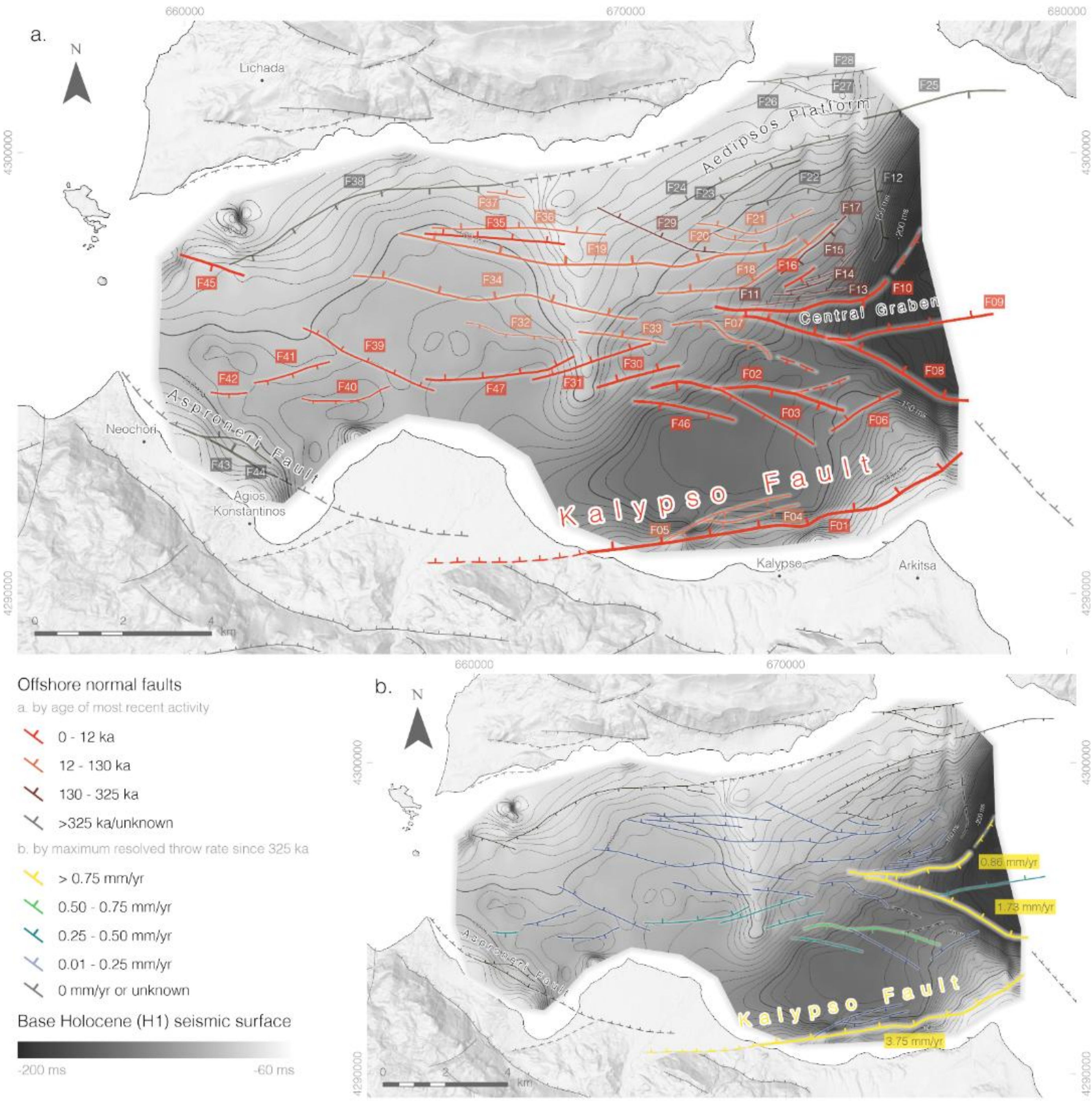

1181

1182 **Figure 7:** Map of offshore fault network identified in this study on depth to base Holocene

1183 (H1), effectively showing pre-Holocene basin geometry (without tectonic or compactional

1184 subsidence correction). a) Faults coloured by most recent activity based on offset of youngest

1185 key seismic horizon outlined in Figure 6. b) Faults coloured by maximum resolved throw rate

1186 over a given interval since ~325 ka (H3) based on throw rates calculated for each key seismic horizon (H1-3). See Supplementary Figure S3 for detail on the generation the H1 surface and Supplementary Table S1 and S2 for further detail on each mapped structure.

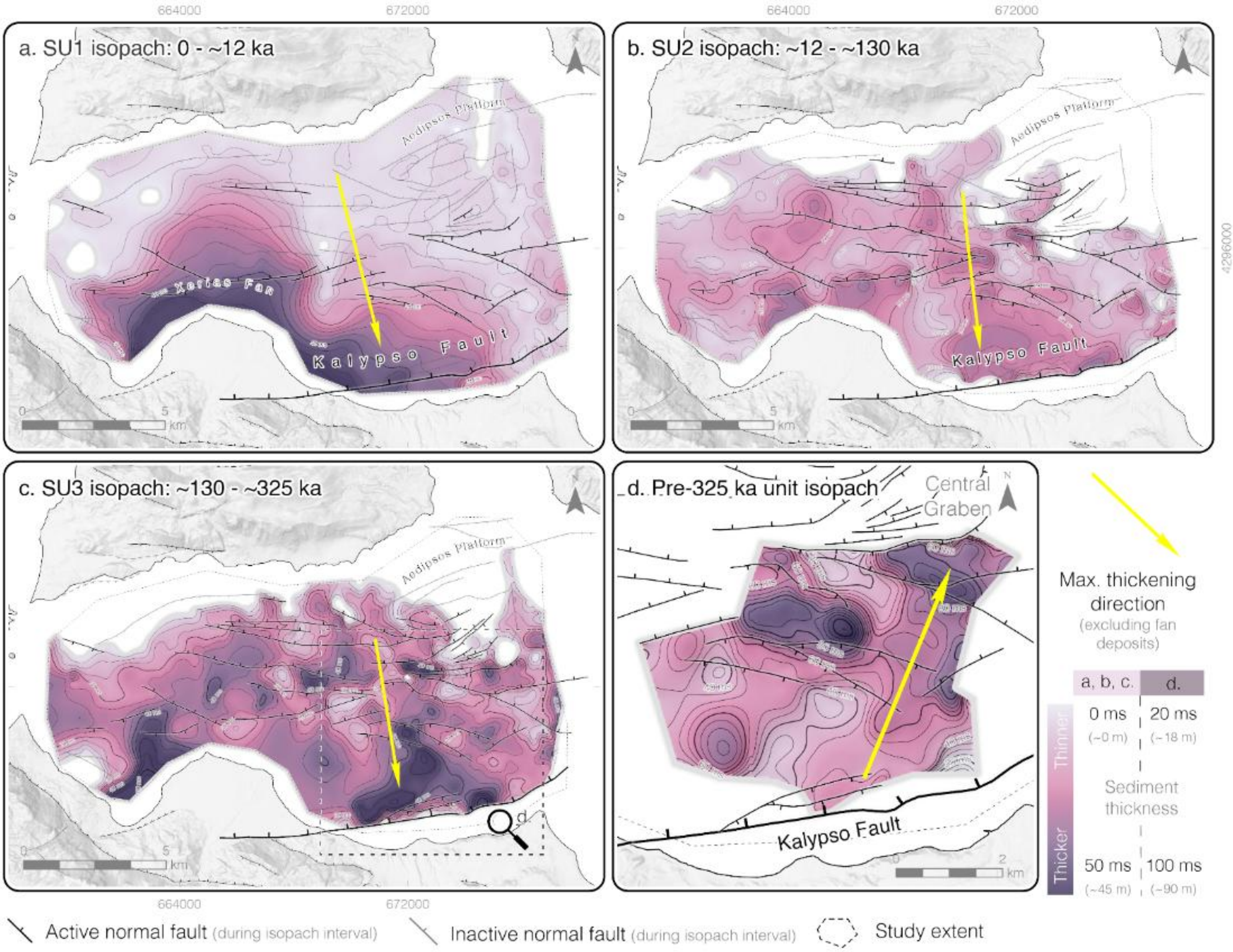

Figure 8: Isopach maps showing sediment thickness between the three major mapped surfaces in this study (a, b and c) and a package underlying the ~325 ka surface that is only apparent in the southeast of the study area (d). White area within study boundary indicates zero thickness.

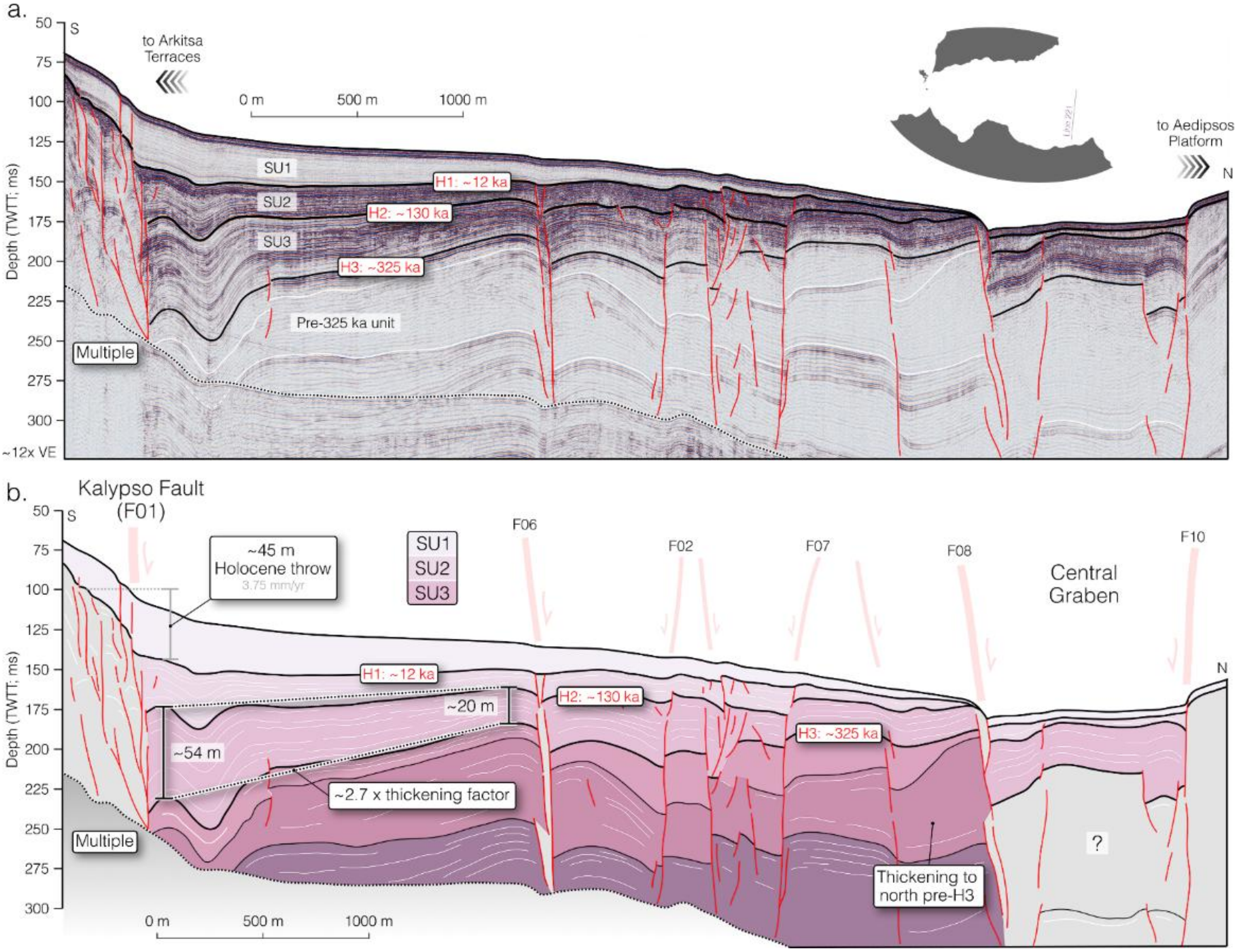

Figure 9: a) Seismic reflection Line 221 with key surfaces (H1-3), seismic units (SU1-3) and faults shown. b) Interpreted section of line 221. The major Kalypso Fault Zone is shown in the south and active Central Graben in the north. SU1-3 thicken towards the Kalypso Fault (south), older packages with unassigned ages thicken towards the Central Graben (north). See Supplementary Figure S10 for uninterpreted seismic section.

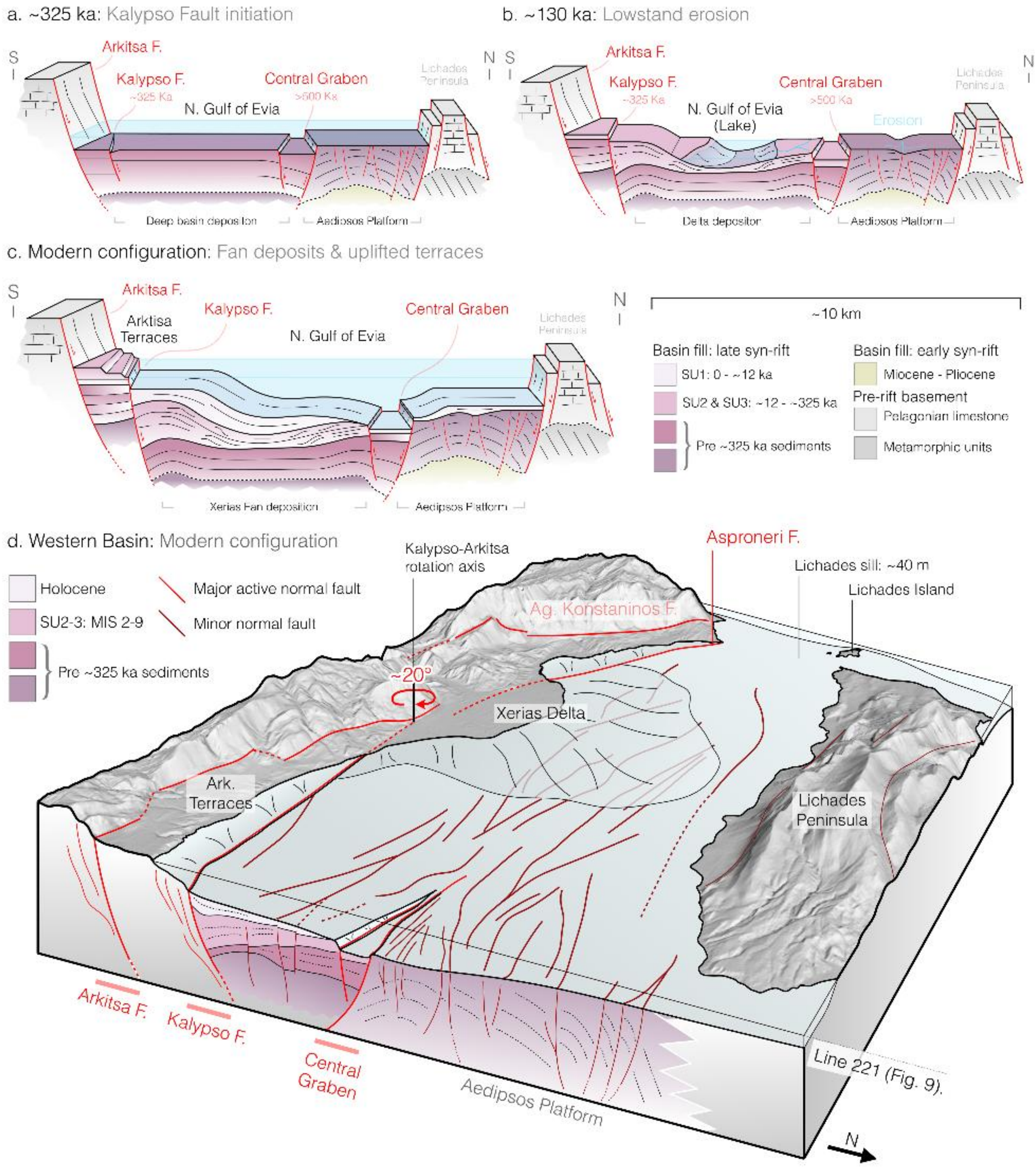

Figure 10: a-c) Schematic evolutionary block models showing structural and sedimentary development of the Western Basin near Arkitsa at ~325 ka (MIS 9e; b), ~130 ka (late-MIS 6; c) and the modern configuration of the basin (d). a) Three-dimensional summary model of the modern Western Basin of the North Gulf of Evia showing fault network, key structures and

modern topography. 2x vertical exaggeration. Cross-section not to scale. Looking towards 240° at 25° pitch.